Monthly Weather Review

VOLUME 99, NUMBER 5

MAY 1971

UDC 551.589:551.513.1:551.511.33:556.1(100)

SIMULATION OF CLIMATE BY A GLOBAL GENERAL CIRCULATION MODEL

I. Hydrologic Cycle and Heat Balance

J. LEITH HOLLOWAY, JR., and SYUKURO MANABE

Geophysical Fluid Dynamics Laboratory, NOAA, Princeton, N.J.

ABSTRACT

The primitive equations of motion in spherical coordinates are integrated with respect to time on global grids with mean horizontal resolutions of 500 and 250 km. There are nine levels in the models from 80 m to 28 km above the ground. The models have realistic continents with smoothed topography and an ocean surface with February water temperatures prescribed. The insolation is for a Northern Hemisphere winter. In addition to wind, temperature, pressure, and water vapor, the models simulate precipitation, evaporation, soil moisture, snow depth, and runoff. The models were run long enough beyond a state of quasi-equilibrium for meaningful statistics to be obtained. Time means of meteorological and hydrological quantities computed by the models compare favorably with observed climatic means. For example, the thermal structure of the model atmosphere is very similar to that of the actual atmosphere except in the Northern Hemisphere stratosphere; and the simulated distributions of the major arid regions over continents and the distributions of the rain belts, both in the Tropics and in middle latitudes, are successfully simulated by the models described in this paper. The increase in the horizontal computational resolution improved the distributions of mean surface pressure and precipitation rate in particular.

CONTENTS

1. INTRODUCTION

The first objective of general circulation modeling experiments is the simulation of climate on a continental, hemispheric, or global scale. Once this initial goal has been achieved to a reasonable degree of faithfulness to reality, the more interesting and enlightening goal can be pursued, which is the use of these models for studying the physical mechanisms that create and maintain climate. This is accomplished by controlled experiments in which some of the defining parameters of the model are changed while others are kept constant. In this way, meteorology may become an empirical science in a manner similar to the field of experimental chemistry where different substances are mixed in a laboratory to learn about various chemical reactions. Modifications can be made to the model that could never even be considered as remotely feasible in nature [e.g., the removal of mountain ranges (Mintz 1968 and Kasahara and Washington 1969) or the elimination of ocean currents (Manabe and Bryan 1969)]. Furthermore, proposed methods for climate modification can be tested in atmospheric models without the tremendous expense and risk involved in testing them in the real atmosphere. Some ideas can be disposed of as useless even without the cost of research into methods for making their application inexpensive enough to be feasible. Finally, theories involving inadvertent modification of weather by human

activity can be tested in general circulation models with greater certainty than by means of statistical studies of atmospheric data spanning the period over which the amount of the particular human activity changed significantly.

Following the pioneering simulations of basic features of the general circulation of the atmosphere by Phillips (1956) and Smagorinsky (1963), various attempts have been made to simulate the global distribution of climate. One important contribution toward this objective was made by Mintz and Arakawa (Mintz 1968) who constructed a general circulation model of the atmosphere with realistic topography and sea-surface temperatures as lower boundary conditions and successfully simulated the essential features of the global distribution of surface pressure. Their model, however, does not include a hydrologic cycle that strongly controls the atmospheric circulation. On the other hand, Leith (1965) and Washington and Kasahara (1970) incorporated into their models the effects of condensation, but these models do not take into consideration one of the most important climatic processes (viz, the water balance of the earth's surface).

Previous to this study, attempts have been made to incorporate moist processes into general circulation models of the atmosphere at the Geophysical Fluid Dynamics Laboratory (GFDL) of NOAA. For example, Manabe et al. (1965) constructed a hemispheric model in which the effects of both evaporation and precipitation were taken into consideration. By using this model, they were successful in simulating some of the features of the hydrologic cycle such as the tropical rain belt, the subtropical dry belt, and the rain belt of middle latitudes (see also Manabe and Smagorinsky 1967). Their model was, however, highly simplified, having neither land-sea contrast nor mountains. Instead, it had a flat moist surface with no heat capacity, which can be perhaps visualized as a very shallow swamp. Following this preliminary study, Manabe (1969) incorporated a computation scheme of ground hydrology into a general circulation model with idealized continents and oceanic areas in a limited domain. His success in simulating some of the fundamental features of the hydrologic cycle, despite the extreme idealization of the geography and of the computation scheme of hydrology, encouraged us to attempt this present study of the numerical simulation of the hydrologic cycle on a global scale.

For making a global atmospheric model, it is necessary to design a grid system that covers the whole globe. Such a grid system was proposed by Kurihara (1965). Using this system, Kurihara and Holloway (1967) successfully performed a numerical time integration of a global model without moist processes and laid the foundation for the present study.

The models described in this paper, therefore, represent the most advanced stage in a series of atmospheric models developed at GFDL during the last 14 yr. The evolution of these models can be traced by referring to some previous papers [1] by the GFDL staff. For the benefit of the reader who does not wish to make such an extensive literature search, we are presenting in the next section a moderately detailed description of the current models.

In the remainder of this paper, we shall describe the results obtained from time integrations of these models with respect to simulating the global distributions of climate and hydrologic elements. Since it is not reasonable to cover all aspects of our results in one paper, special emphasis is placed here on the discussion of the balance of heat and water in the earth-atmosphere system of the model. The general circulation and energetics of disturbances in the model Tropics have already been discussed by Manabe et al. (1970*b*). A detailed discussion of the model's flow field and the effects of mountains (Manabe and Holloway 1971) will be published. A synopsis of some of the hydrologic results, as they pertain to climate modification, has been presented in Manabe and Holloway (1970*a*). Some of these results, applying to the future development of hydrologic models, were presented in Manabe and Holloway (1970*b*).

2. DESCRIPTION OF THE MODEL

A. EQUATIONS OF MOTION

In deriving the equations of motion, we adopted the so-called "σ coordinate" system in which the pressure, normalized by surface pressure, is chosen as the vertical coordinate (Phillips 1957). Making the hydrostatic assumption, we may write the momentum equations on a spherical surface as

$$\frac{\partial}{\partial t}(p_* u) = -D_3(u) + \left(f + \frac{\tan\theta}{a} u\right) p_* v - \left[RT \frac{\partial p_*}{a \cos\theta \partial\lambda} + p_* \frac{\partial \phi}{a \cos\theta \partial\lambda}\right] + {}_H F_\lambda + {}_V F_\lambda \quad (1)$$

and

$$\frac{\partial}{\partial t}(p_* v) = -D_3(v) - \left(f + \frac{\tan\theta}{a} u\right) p_* u - \left[RT \frac{\partial p_*}{a \partial\theta} + p_* \frac{\partial \phi}{a \partial\theta}\right] + {}_H F_\theta + {}_V F_\theta \quad (2)$$

where u and v are the eastward and northward components of the wind, respectively; p_*, surface pressure; σ, pressure normalized by surface pressure; T, temperature; ϕ, geopotential height; θ, latitude; λ, longitude; a, radius of the earth; f, the Coriolis parameter; R, the gas constant for air; and ${}_H\mathbf{F}$ ${}_V\mathbf{F}$ are the frictional forces due to subgrid scale mixing in the horizontal and vertical directions, respectively (see section 2E for details of these frictional terms). The three-dimensional divergence operator $D_3(\ )$ is defined by

$$D_3(\ ) = D_2(\ ) + \frac{\partial[(\ ) p_* \dot{\sigma}]}{\partial\sigma} \quad (3)$$

where $\dot{\sigma}$ denotes the individual change of normalized pressure σ, and

$$D_2(\ ) = \frac{\partial[(\ ) p_* u]}{a \cos\theta \partial\lambda} + \frac{\partial[(\ ) p_* v \cos\theta]}{a \cos\theta \partial\theta}. \quad (4)$$

[1] Smagorinsky 1963, Manabe and Strickler 1964, Smagorinsky et al. 1965, Manabe et al. 1965, Manabe and Wetherald 1967, Kurihara and Holloway 1967, Manabe 1969

The continuity equation may be written as

$$\frac{\partial p_*}{\partial t} = -D_3(1). \tag{5}$$

Integration of eq (5) with respect to σ yields the following prognostic equation for surface pressure:

$$\frac{\partial p_*}{\partial t} = -\int_0^1 D_2(1)d\sigma. \tag{6}$$

The vertical σ and p velocities can be obtained from the diagnostic relations

$$\dot{\sigma} = p_*^{-1}\left[\sigma\int_0^1 D_2(1)d\sigma - \int_0^\sigma D_2(1)d\sigma\right] \tag{7}$$

and

$$\omega = p_*\dot{\sigma} + \sigma\left[\frac{\partial p_*}{\partial t} + u\frac{\partial p_*}{a\cos\theta\partial\lambda} + v\frac{\partial p_*}{a\partial\theta}\right]. \tag{8}$$

The vertical p velocity, ω, is necessary for computing the adiabatic heating (or cooling) term in the thermodynamic equation. It was found that the use of the finite-difference representation of eq (8) caused serious computational difficulties. Therefore, the form of eq (8) is somewhat modified for the actual computation (see appendix A for further details of this modification).

The geopotential height can be obtained by integrating the following hydrostatic equation with respect to σ:

$$\frac{\partial\phi}{\partial\sigma} = -\frac{RT}{\sigma} \tag{9}$$

(note that the equation of state for a perfect gas is used for deriving this equation). The prognostic equation of temperature (i.e., the thermodynamic equation) is described in subsection 2C.

B. FINITE-DIFFERENCE GRID SYSTEM

The model equations are integrated with respect to time by a finite-difference scheme based on the so-called "box" method. The grid system used for the model is identical to that used by Kurihara and Holloway (1967) with the exception that the two, circular polar points have been eliminated by annexation to the surrounding four boxes which become pie-shaped in the process. There are 2,304 grid points at the centers of 2,304 boxes covering the globe. One octant of the grid is shown in figure 1. The rectangles surrounding the grid points represent plan views of rectangular parallelepipeds (or simply boxes) centered on the grid points. Notice that the boxes at one latitude are staggered with respect to those at adjacent latitudes. There are 24 grid points between the Poles and the Equator and 96 points around the Equator. The north-south grid distance is 417 km everywhere; and in the east-west direction, the spacing varies from 417 km at the Equator to 650 km near the Poles.

In the box method, the nonlinear components of the tendencies of pressure, wind, temperature, and humidity are functions of the flux divergence of mass, momentum, heat, and water vapor computed at each box. The resulting computed tendencies are extrapolated in time by the so-called "leapfrog" method. For further details on the method of time integration of the model equations, see appendix A for a discussion of several finite-difference problems that had to be solved to integrate the model experiment successfully.

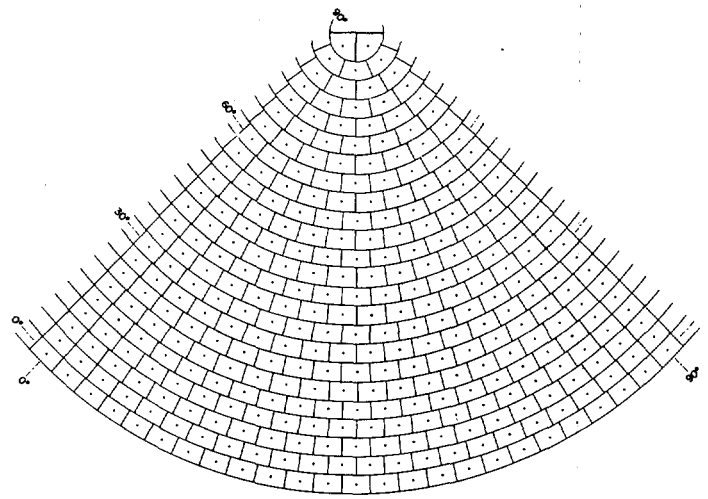

FIGURE 1.—Diagram of one octant of the low resolution (N24) computational grid. Map projection is not conformal.

The model has nine unevenly spaced levels in the vertical from the lowest at about an 80-m height up to a top level at approximately 28 km above the ground. As pointed out in the previous subsection, the σ coordinate system is used to facilitate the incorporation of mountains into the model. In this σ system, the levels are surfaces of constant ratio of pressure to surface pressure. A tabulation of the σ levels and their approximate elevations above the surface points at sea level is shown in table 1 in which data are included for half levels interspersed between the nine integer levels of the model. The vertical σ velocity is defined at these half levels. The derivation of the smoothed topography used in these model experiments is described in appendix C.

TABLE 1.—*The σ levels and their approximate elevations above the surface points at sea level*

Level	$\sigma = p/p_*$	Height (m)
0.5	0.00000000	∞
1.0	.01594441	27,900
1.5	.04334139	21,370
2.0	.07000000	18,330
2.5	.11305591	15,290
3.0	.16500000	12,890
3.5	.24081005	10,500
4.0	.31500000	8680
4.5	.41204675	6860
5.0	.50000000	5430
5.5	.60672726	4010
6.0	.68500000	3060
6.5	.77337055	2110
7.0	.83500000	1490
7.5	.90154066	860
8.0	.94000000	520
8.5	.98010000	170
9.0	.99000000	80
9.5	1.00000000	0

C. THERMODYNAMICS AND RADIATION

The model's temperature tendency equation based on the thermodynamic equation is

$$\frac{\partial}{\partial t}(p_* T) = -D_3(T) + \frac{R}{c_p}\frac{T\omega}{\sigma} + \left[\frac{\partial(p_* T)}{\partial t}\right]_C + \left[\frac{\partial(p_* T)}{\partial t}\right]_{RAD} + {}_H F_T \quad (10)$$

where c_p is the specific heat of air under constant pressure and ${}_H F_T$ represents the contribution of the horizontal subgrid scale mixing discussed in subsection 2E. The first term on the right-hand side of eq (10) computes the warming or cooling resulting from the large scale three-dimensional flux divergence of heat. The second term gives the adiabatic temperature change produced by large-scale vertical motion. The third and fourth terms represent the heating (or cooling) by condensation or convective processes and by radiation, respectively.

The scheme for computing the convective temperature changes consists of a so-called "moist convective" adjustment and a "dry convective" adjustment. Since the former is described in the following subsection, we shall describe only the latter here. The dry convective adjustment is performed if the lapse rate given by the other terms in the thermodynamic equation is super dry-adiabatic. The lapse rate is adjusted to the dry-adiabatic lapse rate so as to simulate the effects of strong mixing by dry convection in the free atmosphere. This adjustment is performed in the model in such a way that the sum of potential and internal energies are conserved.

The scheme for computing the radiative heating and cooling is identical to that described by Manabe and Strickler (1964) and Manabe and Wetherald (1967). It was incorporated, for example, in the GFDL stereographic models described in Smagorinsky et al. (1965) and Manabe et al. (1965). The computation scheme consists of two parts (viz, a part for longwave radiation and one for solar radiation). The principles of computing the flux of longwave radiation are not very different from those adopted for constructing a so-called "radiation" diagram such as the one proposed by Yamamoto (1952). (Stone and Manabe 1968 compared the flux of longwave radiation obtained by this method with those obtained by various methods proposed by other authors.)

The insolation at the top of the atmosphere is for a Northern Hemisphere winter and did not change during the entire time integration of the model. For simplicity, the diurnal variation of solar radiation is eliminated by use of the effective mean zenith angle for each latitude. The gaseous absorbers, taken into consideration for the computation of both solar and terrestrial radiation, are water vapor, carbon dioxide, and ozone. In addition, the effects of clouds are incorporated into the scheme. As in previous GFDL models, the distribution of mixing ratio computed by the prognostic equation of water vapor is not used for the computation of radiative transfer. Instead, we used the climatic distributions of water vapor in the troposphere for the months of December, January, and February, which are determined by a method based upon studies by Telegadas and London (1954) and by Murgatroyd (1960). The mixing ratio of the upper troposphere is assumed to be smoothly connected to the stratospheric value of a mixing ratio of 3×10^{-6} g water vapor/g air, as suggested by Mastenbrook (1965). The distribution of ozone is determined from ozone measurements by Hering and Borden (1965). Their total amounts are normalized in such a way that they coincide with the distributions compiled by London (1962) who used extensive measurements of total ozone by means of a Dobson spectrometer. For the computation of the radiative transfer, the distributions of both water vapor and ozone are specified to be functions of latitude and height but not of longitude. On the other hand, the mixing ratio of carbon dioxide is assumed to have a constant value of 0.0456 percent by weight everywhere. Clouds are classified into three categories (viz, high, middle, and low clouds, including cumuliform). The distribution of these clouds in January is determined by use of the table of cloud amount compiled by London (1957).

The distribution of albedo over oceanic surfaces and for the snow-free surfaces of the continents is specified by referring to the distributions of albedo compiled by Posey and Clapp (1964). The albedos of the grid points where snow cover is computed are determined by a method based on a study by Kung et al. (1964). According to their results, the surface albedo is a function of snow depth because exposed patches not covered by snow decrease in both size and number as the snow depth increases. Figure 3 of their paper shows that the difference between the albedo of bare soil and that of a snow-covered surface is approximately proportional to the square root of the snow depth if the snow depth is less than 10 cm. When the snow depth exceeds 10 cm, the value of the surface albedo becomes almost independent of snow depth. Based on their results, the following formulas were derived for computing the albedo of snow-covered surfaces:

$$A = A_b + (S_w)^{1/2}\cdot(A_s - A_b), \text{ if } S_w < 1 \text{ cm}, \quad (11)$$

and

$$A = A_s, \quad \text{if } S_w \geq 1 \text{ cm}, \quad (12)$$

where A_b and A_s are the albedos of bare soil and of deep snow, respectively, and A is the albedo of the earth's surface covered by snow of water equivalent S_w, assumed here to be one-tenth of the snow depth. For our computations, A_s is assumed to be 0.60. Poleward of latitude 75°, however, the albedo over land and pack ice is assumed to be 0.75 everywhere, as suggested by the results of Kung et al. (1964).

D. MOIST PROCESSES

The tendency equation used for predicting mixing ratios in the model is

$$\frac{\partial}{\partial t}(p_* r) = -D_3(r) + \left[\frac{\partial(p_* r)}{\partial t}\right]_C + {}_H F_r + {}_V F_r. \quad (13)$$

The first term in eq (13) gives the contribution to the mixing ratio change, resulting from the three-dimensional flux divergence of water vapor. The second term stands for the effects of moist convective adjustment and condensation. The third and fourth terms represent the contributions of the horizontal and vertical subgrid scale mixing, respectively. These last two terms are discussed further in subsection 2E. If in the numerical evaluation of this equation truncation error causes a negative mixing ratio at any layer, this erroneous value is set to zero. Whenever possible, moisture is borrowed from adjacent layers in the column to make up this deficit of water vapor in such a way as to satisfy the water balance over the entire domain.

One of the most serious difficulties in designing a numerical model of the general circulation is in the parameterization of moist convection. Since we know very little about the interaction of small-scale convection with the large-scale fields of motion, we adopted an extremely simple system for simulating the effect of moist convection on the macroscopic behavior of the atmosphere. Despite its simplicity, this system qualitatively possesses at least some of the essential characteristics of moist convection in the actual atmosphere. The basic assumptions adopted for this system of moist convection are:

1. If air is saturated and the lapse rate is super moist-adiabatic, free convection is strong enough to make the equivalent potential temperature uniform and the relative humidity saturated in the convective layer.
2. The sum of potential, internal, and latent energy is conserved during the convective adjustment.

The net effect of this moist convection scheme in the model is to neutralize the lapse rate, release the heat of condensation, and transfer heat from the lower to the upper layers.

More specifically, the tendency equations for temperature and mixing ratio are first evaluated without the convective adjustment terms, and the resulting tendencies are extrapolated in time to obtain tentative values of temperature and mixing ratio at the next time step. If the combination of these temperatures and mixing ratios at two or more adjacent levels defines a super moist-adiabatic lapse rate in the presence of saturated or supersaturated air, free convection of sufficient intensity is assumed to take place to produce a uniform equivalent potential temperature and a saturated humidity in the layers associated with these levels in the model. Excess moisture is condensed, and the integral of this condensation over the entire column of air above a grid point is counted as the precipitation amount. For each moist unstable layer containing n contiguous levels of the model, the n temperature and n mixing ratio corrections are determined from the solution of $2n$ simultaneous equations derived from n saturation mixing ratio versus temperature relations, $n-1$ neutral moist lapse rate conditions, and one integral energy conservation requirement based on assumption (2). Further details of the moist convective scheme may be found in Manabe et al. (1965).

If the tentative lapse rate is not super moist-adiabatic, condensation will still be forecast to occur in the model atmosphere whenever and wherever the tentative mixing ratio exceeds the saturation value. At each supersaturated level, incremental changes of temperature and mixing ratio are determined from the simultaneous solution of a pair of equations by an iterative method. For simplicity in the computation scheme, all condensation resulting from this procedure is assumed to fall out of the atmosphere immediately, and no condensation goes into clouds or evaporates while falling through drier lower layers. Differentiation between rain or snow depends upon the temperature at a height of about 350 m. This height is selected subjectively by reference to a survey article by Penn (1957). If the temperature at this level is freezing or below, snow is forecast; otherwise, rain is predicted.

E. SUBGRID SCALE VERTICAL AND HORIZONTAL MIXING

The formulation of the vertical mixing of momentum used in this work is identical to that described by Smagorinsky et al. (1965). The frictional force produced by this vertical mixing of momentum is computed by

$$\frac{{}_V\mathbf{F}}{p_*}=\frac{1}{\rho}\frac{\partial {}_V\tau}{\partial z}=-\frac{g}{p_*}\frac{\partial {}_V\tau}{\partial \sigma} \tag{14}$$

where ρ and g are the density of air and the acceleration of gravity, respectively. The components of the vector ${}_V\mathbf{F}$ are ${}_VF_\lambda$ and ${}_VF_\theta$ appearing in eq (1) and (2). The stress on a horizontal surface ${}_V\tau$ is computed by

$${}_V\tau=\rho K_V\frac{\partial \mathbf{V}}{\partial z} \tag{15}$$

where the coefficient of vertical diffusion, K_V, is based on the mixing length hypothesis, namely,

$$K_V=l^2\left|\frac{\partial \mathbf{V}}{\partial z}\right|. \tag{16}$$

The mixing length l is assumed to increase linearly with respect to height up to 75 m and then to decrease linearly with height to 2.5 km where it becomes zero. Therefore, no subgrid scale vertical mixing is assumed to occur above 2.5 km. The value of l at 75 m is assumed to be 30 m (this implies that the Kármán constant is equal to 0.4 below 75 m). The equation for computing the stress at the lower boundary is presented in subsection 2F.

The vertical diffusion of mixing ratio in this model is the same as described by Manabe et al. (1965). The change in mixing ratio, resulting from small-scale vertical

mixing, is given by

$$_{V}F_{r}=\frac{p_*}{\rho}\frac{\partial W}{\partial z} \tag{17}$$

where

$$W=\rho K_V\frac{\partial r}{\partial z}. \tag{18}$$

For computational stability, the vertical diffusion equations are solved implicitly by a method described by Richtmyer (1957).

No attempt is made to incorporate a vertical diffusion of heat other than to compute the sensible heat flux at the surface of the earth. Since we incorporated the vertical mixing of momentum and mixing ratio, this mechanism for vertical mixing of heat should have been incorporated into the model for consistency. However, the effects of the dry and moist convective adjustments are so large in most areas that the omission of this type of mixing does not make a significant difference. It is, therefore, felt that the dry and moist convective adjustments provide the model with adequate small-scale vertical mixing of heat.

The formulation of the horizontal subgrid scale mixing is an adaptation of the scheme used by Smagorinsky et al. (1965). According to Smagorinsky (1963), the rates of change of the east-west and north-south momentum, resulting from the horizontal stresses appearing in eq (1) and (2), are computed as

$$_{H}F_{\lambda}=\frac{\partial\tau^{\lambda\lambda}}{a\cos\theta\partial\lambda}+\frac{\partial(\tau^{\lambda\theta}\cos^2\theta)}{a\cos^2\theta\partial\theta} \tag{19}$$

and

$$_{H}F_{\theta}=\frac{\partial\tau^{\theta\lambda}}{a\cos\theta\partial\lambda}+\frac{\partial(\tau^{\theta\theta}\cos\theta)}{a\cos\theta\partial\theta}+\frac{\tan\theta}{a}\tau^{\lambda\lambda} \tag{20}$$

where $\tau^{\lambda\lambda}$, $\tau^{\lambda\theta}$, $\tau^{\theta\lambda}$, and $\tau^{\theta\theta}$ denote the stress tensors resulting from mixing along constant σ surfaces. Ignoring the density variation on a constant σ surface and assuming the hydrostatic relationship, we can express the stress tensors by

$$\tau^{\lambda\lambda}=-\tau^{\theta\theta}=p_*K_HD_T \tag{21}$$

and

$$\tau^{\lambda\theta}=\tau^{\theta\lambda}=p_*K_HD_S \tag{22}$$

where the tension and shearing rates of strain, respectively, are defined as

$$D_T=\frac{\partial u}{a\cos\theta\partial\lambda}-\frac{\cos\theta}{a}\frac{\partial}{\partial\theta}\left(\frac{v}{\cos\theta}\right) \tag{23}$$

and

$$D_S=\frac{\partial v}{a\cos\theta\partial\lambda}+\frac{\cos\theta}{a}\frac{\partial}{\partial\theta}\left(\frac{u}{\cos\theta}\right). \tag{24}$$

The assumption of an inertial subrange yields the following relation by dimensional analysis:

$$K_H=l_H^2|D| \tag{25}$$

where $|D|=(D_T^2+D_S^2)^{1/2}$ and l_H is a characteristic length corresponding to the scale that defines the exchange coefficient. This length is assumed to be defined as

$$l_H=k_0\delta_s \tag{26}$$

where the parameter k_0 related to the Kármán constant is assigned the value 0.2 in this paper. In the above relation, δ_s is the grid distance in the appropriate direction. For the computations of the rates of strain on the northern and southern grid box interfaces, δ_s is $a\Delta\theta$; on the eastern and western interfaces, $\delta_s=a\cos\theta\Delta\lambda$ where $\Delta\theta$ and $\Delta\lambda$ are the increments of latitude and longitude, respectively, on the grid system. The performance of the nonlinear viscosity described here was extensively discussed by Manabe et al. (1970*a*).

For preventing excessive mixing of heat and moisture along mountain slopes, we assume that these properties are mixed on isobaric instead of on σ surfaces.[2] The approximate equation for computing the contribution of horizontal mixing to the change of temperature or mixing ratio of water vapor is

$$_{H}F_{\alpha}\simeq\frac{\partial}{a\cos\theta\partial\lambda}\left[p_*K_H\left(\frac{\partial\alpha}{a\cos\theta\partial\lambda}\right)_p\right]+\frac{\partial}{a\cos\theta\partial\theta}\left[p_*K_H\cos\theta\left(\frac{\partial\alpha}{a\partial\theta}\right)_p\right] \tag{27}$$

where α stands for either temperature or mixing ratio. For a more general form of this equation, refer to Kurihara and Holloway (1967). In the derivation of eq (27), the more general form of the equation is simplified by the dropping of less important terms for economy in computation. We feel that this approximation does not cause serious error except near steep mountain slopes.

For computational stability, these horizontal mixing computations are performed by using the so-called "forward time differencing" method.

F. BOUNDARY CONDITIONS AT THE EARTH'S SURFACE

The surface stress in the model (τ_*) is computed by

$$(\tau_*)=-\rho(h)C_D(h)|\mathbf{V}(h)|\mathbf{V}(h) \tag{28}$$

where $C_D(h)$ is the drag coefficient applicable to winds at height h and is defined as

$$C_D(h)=\{k_0[\log_e(hz_0^{-1})]^{-1}\}^2 \tag{29}$$

and where $\rho(h)$ is density, $\mathbf{V}(h)$ is the velocity at height h, and k_0 is the Kármán constant. The roughness parameter z_0 is assumed to be 1 cm, and h is chosen to be equal to the height of the lowest prognostic level. The surface stress thus computed constitutes the lower boundary condition for the computation of the Reynolds stress resulting from vertical mixing.

[2] Momentum is not mixed on isobaric surfaces, which is inconsistent with the mixing formulation used here for heat and moisture. However, the difference between results computed by mixing momentum on constant σ instead of on constant pressure surfaces is thought to be small.

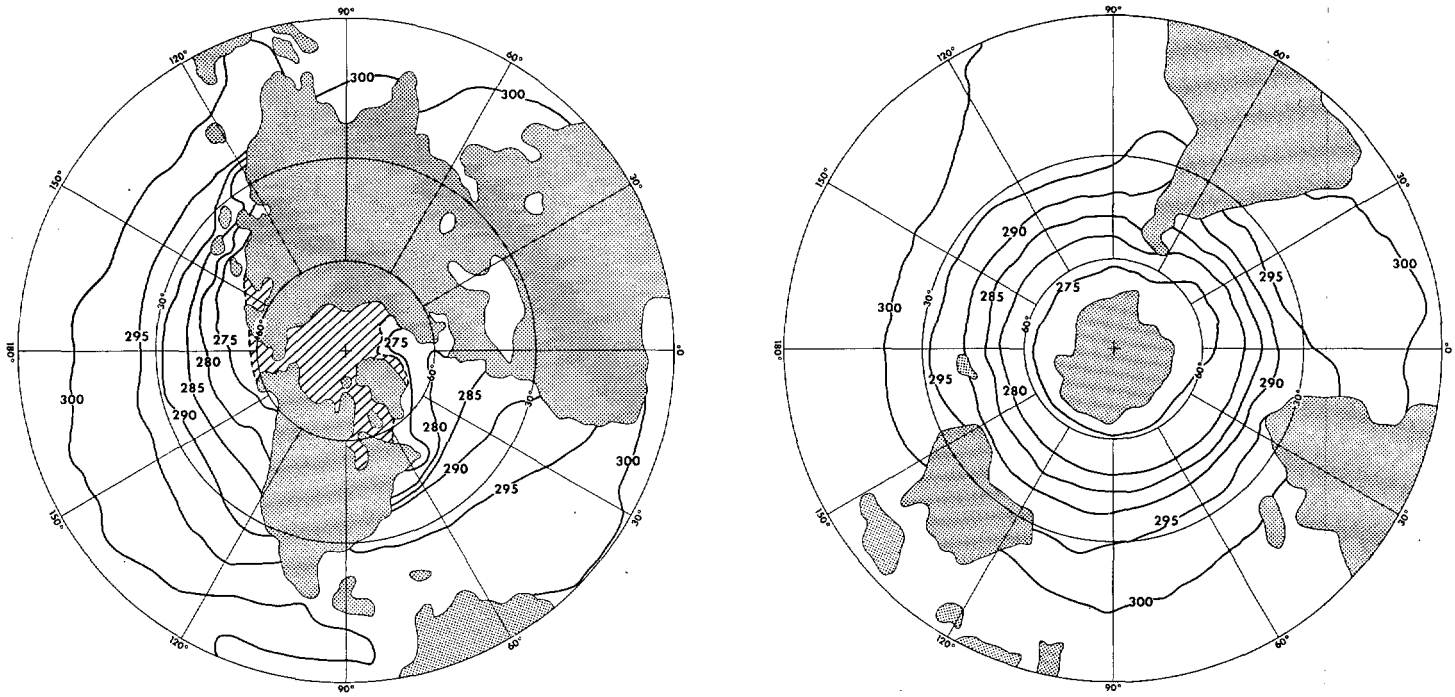

FIGURE 2.—Polar stereographic maps of the prescribed February sea-surface temperatures for the model in the Northern (left) and Southern (right) Hemispheres. The areas of pack ice are shaded with slashed lines, and the continental areas are shaded with dots; units, °K.

Similarly, the heat flux $({}_vH)_*$ at the surface of the earth for either land or sea is given by the relation

$$({}_vH)_* = c_p\rho(h)C_D(h)|\mathbf{V}(h)|\{T_* - T(h)[\sigma(h)]^{-R/c_p}\} \quad (30)$$

where T_* is the surface temperature. For insuring that a minimum amount of heat is exchanged between the earth's surface and the lowest level of the model atmosphere, the wind speed $|\mathbf{V}(h)|$ used in eq (30) is not allowed to be less than 1 m/s.

The flux of latent energy $({}_vLH)_*$ from the ocean is obtained from

$$({}_vLH)_* = LE \quad (31)$$

and

$$E = \rho(h)C_D(h)|\mathbf{V}(h)|[r_s(T_*) - r(h)] \quad (32)$$

where L is the latent heat of evaporation, E is the rate of evaporation, and $r_s(T_*)$ is the saturation mixing ratio of water vapor over water at the surface temperature. Over land, E is computed from eq (32) only when the land surface is sufficiently wet. The formula for estimating the rate of evaporation from a drier surface is discussed in the following subsection. The heat and moisture fluxes at the earth's surface constitute the lower boundary conditions for the computation of the vertical mixing of heat and moisture.

Over land, the temperature of the earth's surface T_* is determined in such a way that it satisfies the requirements of a surface heat balance. If we assume that the heat capacity of the land surface is zero (i.e., no heat conduction into the soil), the equation of the heat balance requirement is

$$S_* + (\mathrm{DLR})_* = \sigma_{SB}T_*^4 + ({}_vH)_* + ({}_vLH)_* \quad (33)$$

where S_* and $(\mathrm{DLR})_*$ are the net downward insolation and the net downward longwave radiation at the earth's surface, respectively, and σ_{SB} is the Stefan-Boltzmann constant. Since the diurnal variation of insolation is eliminated in the model, we assume that it is therefore justifiable to neglect heat conduction into the soil. Equation (33) is solved with respect to T_* numerically. Once T_* is determined, it is then possible to compute the upward flux of both sensible and latent heat from eq (30–32).

Over pack ice, the term Q_{ice} representing heat conduction into or out of the ice is added to the right-hand side of eq (33); thus

$$Q_{ice} = kI^{-1}(T_* - 271.2°\mathrm{K}) \quad (34)$$

where k is the thermal conductivity of ice (assumed to be 5×10^{-3} cal·s^{-1}·cm^{-1}·°C^{-1} in this study) and I is the ice thickness taken to be 2 m in the ice-covered area specified in figure 2. We considered 2 m as a representative thickness of sea ice in the Arctic (in the Southern Hemisphere summer, sea ice is of negligible extent around the Antarctic). The temperature of the sea water below the pack ice is assumed to be 271.2°K. If the solution to this heat balance equation results in a value of T_* above freezing, this value is set back to freezing with the implicit assumption that the excess heat is used for melting pack ice.

The surface temperature over the oceans is prescribed

as the climatic mean February values determined from U.S. Hydrographic Office (1944) data. See figure 2 for a map of these prescribed sea temperatures.

G. GROUND HYDROLOGY

One essential part of the hydrologic cycle of the earth-atmosphere system is the storage of water in the ground or on top of the surface as snow. In the design of the scheme for computing the ground hydrology, we desired to make this procedure very simple for two reasons:

1. For ease in interpretation of the results, it is advisable to try a rather simple scheme before using a very sophisticated one.
2. These computations have to be performed at a great number of grid points, which dictates that the most efficient method must be used, lest the hydrologic calculations take an inordinate amount of computer time.

The procedure incorporated into the model is highly idealized and is the same as used by Manabe (1969). The reader should refer to this reference for more details of this system and for some of the justifications for our simplifying assumptions.

The maximum amount of water that can be stored in the ground is called the field capacity of the soil of a particular area. The field capacity of soil, of course, depends upon a number of characteristics of the ground surface and thus varies considerably throughout the world, the domain of this global general circulation model. For the utmost simplicity in our first attempt to model the ground hydrology on a global scale, we have set the field capacity of the soil to 15 cm over all land areas. Most of the time, the actual soil moisture at a given point falls short of the field capacity of the soil in that area. In the model, a budget of soil moisture is kept at each land grid point. Over all land points, the soil moisture was initially set to its full capacity of 15 cm. Changes in soil moisture are computed as the residual of contributions from processes that increase soil moisture (i.e., rainfall and snowmelt) and those that decrease it (i.e., evaporation and runoff). Runoff is predicted at a grid point only if a forecast change in soil moisture would result in a water depth exceeding the field capacity. Implicit in this procedure is the assumption that the rate of infiltration of water into the soil is always greater than the sum of the rainfall and snowmelt rates, as long as the field capacity of the soil is not exceeded. Any moisture above 15 cm is thus computed as runoff at the grid point where this occurs. Runoff is assumed to flow directly to the sea via rivers without affecting the soil moisture at any other point.

The effect of soil moisture on evaporation is incorporated into the model by a simple scheme used by Budyko (1956). When the soil does not contain a sufficient amount of water, the amount of evaporation is smaller than the value obtained from eq (32), which gives the evaporation from the sea or a perfectly wet surface. Equation (32) thus gives an upper limit for evaporation over a land surface. This upper limit is termed "evaporability" or "potential evaporation." If the soil moisture is greater than a certain critical percentage (75 in this study) of the maximum soil capacity, evaporation is assumed to equal evaporability. Otherwise, evaporation from land is computed to be linearly proportional to soil moisture up to this critical value. Over snow or ice, the sublimation also equals evaporability; but in the computation of the latter, $r_s(T_*)$ is the saturation mixing ratio of water vapor over ice instead of over water in eq (32), and L is now the latent heat of sublimation in eq (31).

The equation for the prediction of the water equivalent depth of snow S is

$$\frac{\partial S}{\partial t}=S_r-E-M_e \tag{35}$$

where S_r is the rate of snowfall, M_e is the rate of snowmelt, and E is the sublimation rate. The snowmelt rate may be calculated from a heat balance condition at the snow-covered surface as

$$\begin{aligned} &M_e=E_X L_f^{-1}, \text{ if } E_X>0 \\ \text{or}\quad &M_e=0, \qquad \text{if } E_X\leq 0 \end{aligned} \tag{36}$$

where L_f is the latent heat of fusion and E_X, the rate of excess heat energy made available for melting snow, is computed from

$$E_X=[S_*+(\mathrm{DLR})_*-\sigma_{SB}T^4-({}_vH)_*-({}_vLH)_*]_{T_*=273.2^\circ\mathrm{K}} \tag{37}$$

with T_* held constant at freezing [see eq (30) for $({}_vH)_*$ and eq (31) for $({}_vLH)_*$].

After the snow disappears by melting or sublimation, moisture again evaporates from the soil surface. Therefore, it is necessary to keep track of soil moisture even when the ground is covered by snow. We must know the water-holding capacity of snow to do this. The water-holding capacity of snow depends on the snow depth and density and on many other complicating factors, and it ranges from 2 to 5 percent of the weight of the snow according to a study by Gerdel (1954). For simplicity, we shall assume that the moisture-holding capacity of snow is zero. If the soil moisture below a snow cover is less than the field capacity, the rate of increase in soil moisture there equals the sum of the rainfall and snowmelt rates, and the runoff rate is zero. If the soil moisture below the snow equals the field capacity, its value remains at that level, and the runoff is taken to be the sum of the rainfall and snowmelt. Because of the possible effects of freezing, melting, and sublimation of soil moisture, the actual processes could be more complicated than those idealized conditions assumed to occur in our model. Nevertheless, we feel that the scheme described here for computing soil moisture, snowmelt, and runoff represents the elementary features of the hydrologic phenomena at the ground surface.

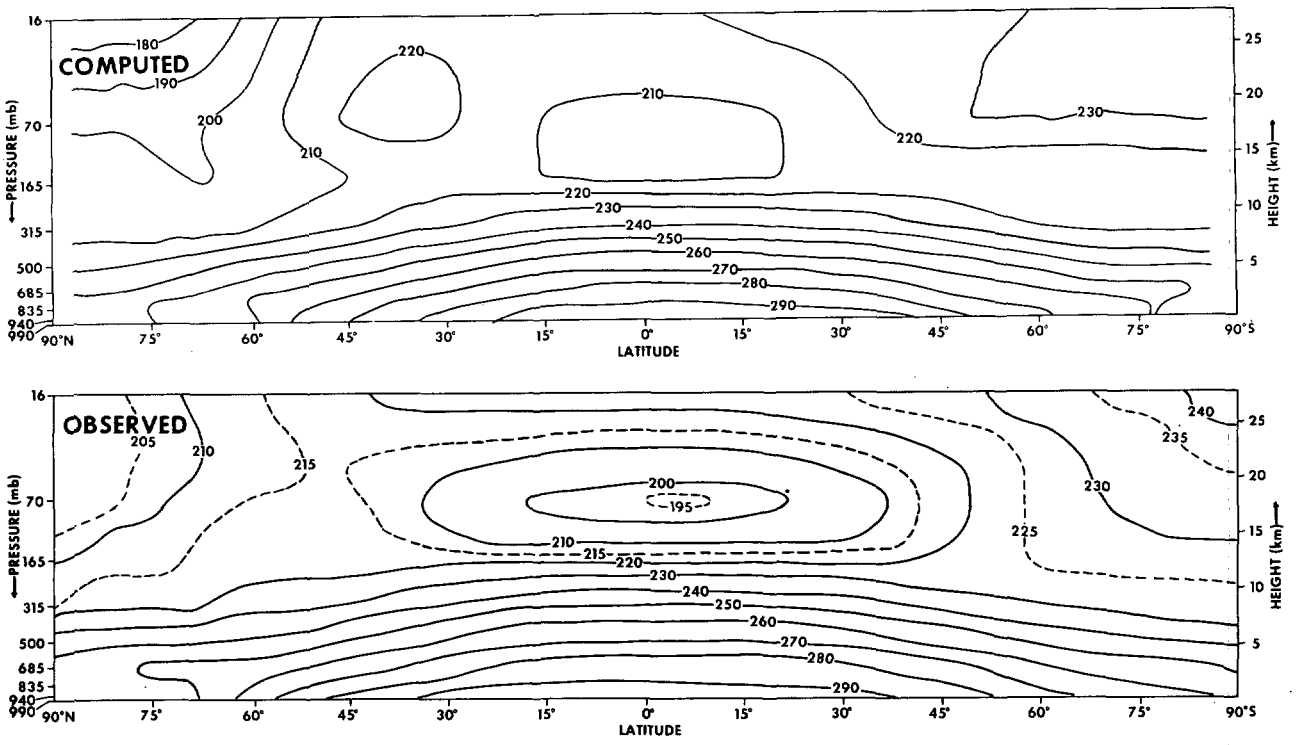

FIGURE 3.—Latitude-height distribution of the mean zonally averaged temperature computed by the N24 model compared with the mean observed distribution for December through February derived by Newell et al. (1969); units, °K.

3. SIMULATION OF CLIMATE BY THE MODEL

The low resolution (N24) model was started from zonally averaged data from a previous model. In general circulation model experiments, about 100 days must be integrated before quasi-equilibrium is reached. As a result of a number of model changes in stream, more than 200 days were required for equilibrium in this model experiment. A total of 341 days was integrated in time. A period of 70 days was averaged for the hydrologic means and another 40-day period was used for the wind and temperature means. Unless otherwise stated, all results presented in this section are for the N24 grid model. See appendix B for a discussion of the high-resolution (N48) model run.

A. TEMPERATURE

Figure 3 shows a 40-day mean latitude-height distribution of the zonally averaged temperature computed by the model compared with the mean observed distribution for the Northern Hemisphere winter. The zonal mean observed temperatures and zonal winds presented in this paper are derived by Newell et al. (1969) for the months of December through February.

In general, the atmospheric temperature distribution computed by the model is similar to the observed except in high latitudes of the winter hemisphere. In the Northern Hemisphere troposphere, high-latitude temperatures are several degrees lower than the observed values, due in part to the perpetual winter there. For example, the temperature of the Arctic is about 10°K too low. This effect in turn pushes the snow line southward. Since the presence of snow increases the albedo above what is normal without snow and the heating of the ground surface by solar radiation is consequently decreased, the extreme winter conditions in the Northern Hemisphere are self-perpetuating by positive feedback and tend to propagate southward.

In the summer stratosphere of the model, the warm Antarctic is simulated successfully. Therefore, the temperature in the lower stratosphere of the model in the Southern Hemisphere increases with latitude, but this increase is not as large as in the real atmosphere. As the results of Manabe and Hunt (1968) indicate, this discrepancy with observation is probably attributable to low vertical resolution in the tropical stratosphere, which smoothes out and thus raises the minimum temperature at the equatorial tropopause. They were able to simulate a sharp tropical tropopause in a time integration of a hemispheric general circulation model, having 18 vertical finite-difference levels, double the number in our model. In the Northern (winter) Hemisphere of the model, the temperature of the lower stratosphere is too low in higher latitudes. It has, nevertheless, a maximum in middle latitudes, in qualitative agreement with features of the actual atmosphere. In section 7, the heat balance of the lower stratosphere is analyzed to determine how the thermal structure of the model stratosphere is maintained.

In figure 4, the observed global distribution of surface ambient air temperature over the entire earth during January is compared with the values of surface tempera-

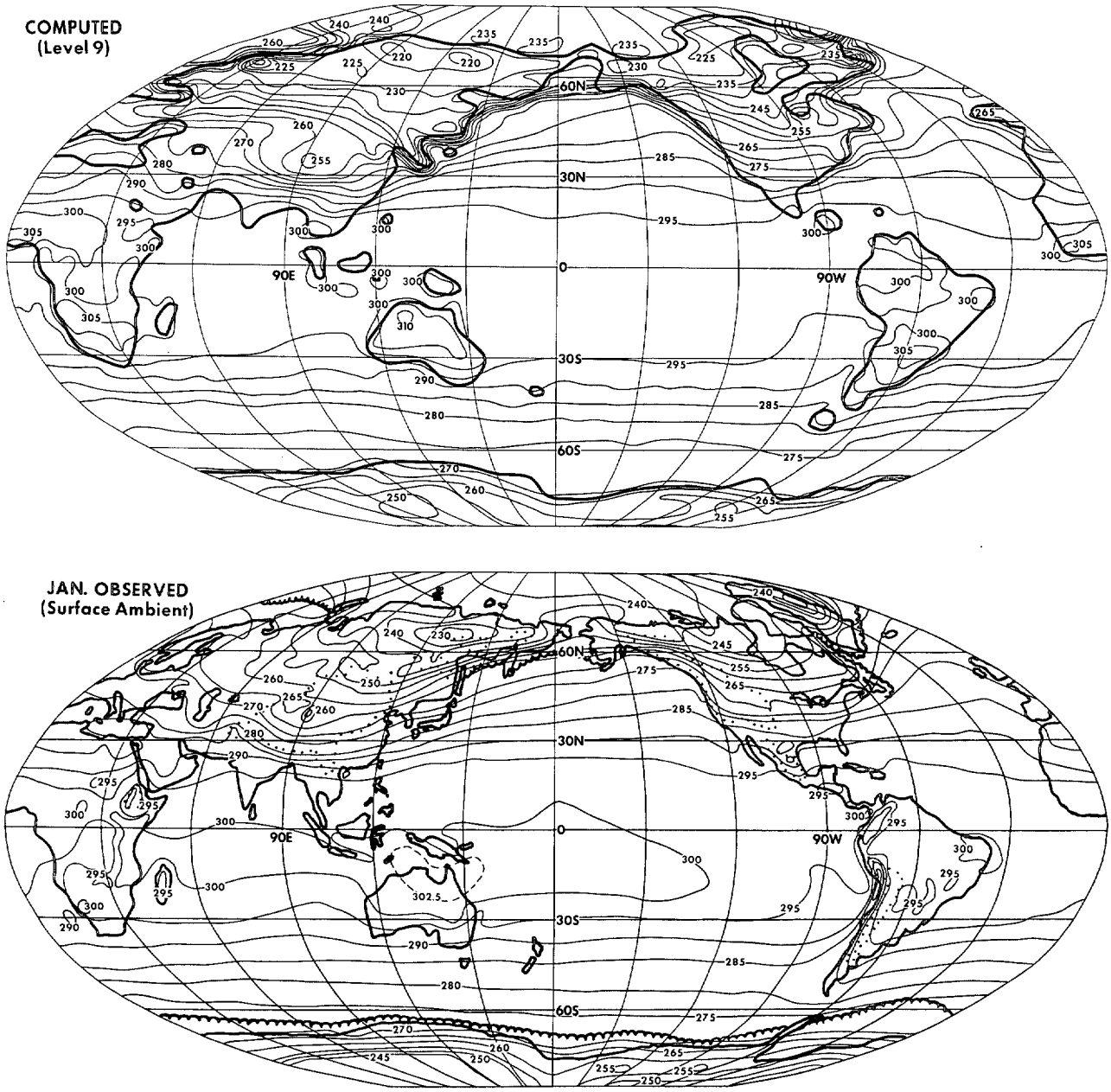

FIGURE 4.—Global distribution of mean temperatures computed in the N24 model experiment for the lowest prognostic level (at a height of about 80 m) compared with the distribution of observed mean surface ambient temperature for January; units, °K. These maps and all those of this type that follow are drawn on a modified elliptical map projection. The dots on the observed map and on later ones outline highland areas.

tures computed by the model experiment for the lowest prognostic level. In the Northern Hemisphere, the observed temperatures are from Crutcher and Meserve (1970); and in the Southern Hemisphere, from Taljaard et al. (1969). In the Northern Hemisphere, the continental temperatures created in the model experiment are somewhat lower than normal because of extensive snow cover extending to low latitudes, attributed to the perpetual winter in this hemisphere. This results in a large temperature contrast between land and sea (e.g., off the east coast of Asia) because the sea-surface temperatures are specified as the climatic values.

In the Southern Hemisphere, surface temperatures computed by the model are very high over Australia and the southern halves of South America and Africa. These temperatures result from the dry soil and produce low relative humidities and low pressures over these regions as described in subsections 3C and 3D.

B. WIND AND MERIDIONAL CIRCULATION

Figure 5 shows the time-mean computed and observed latitude-height distributions of the zonally averaged zonal component of the wind with easterly winds (negative values) shaded. The axes of the computed tropo-

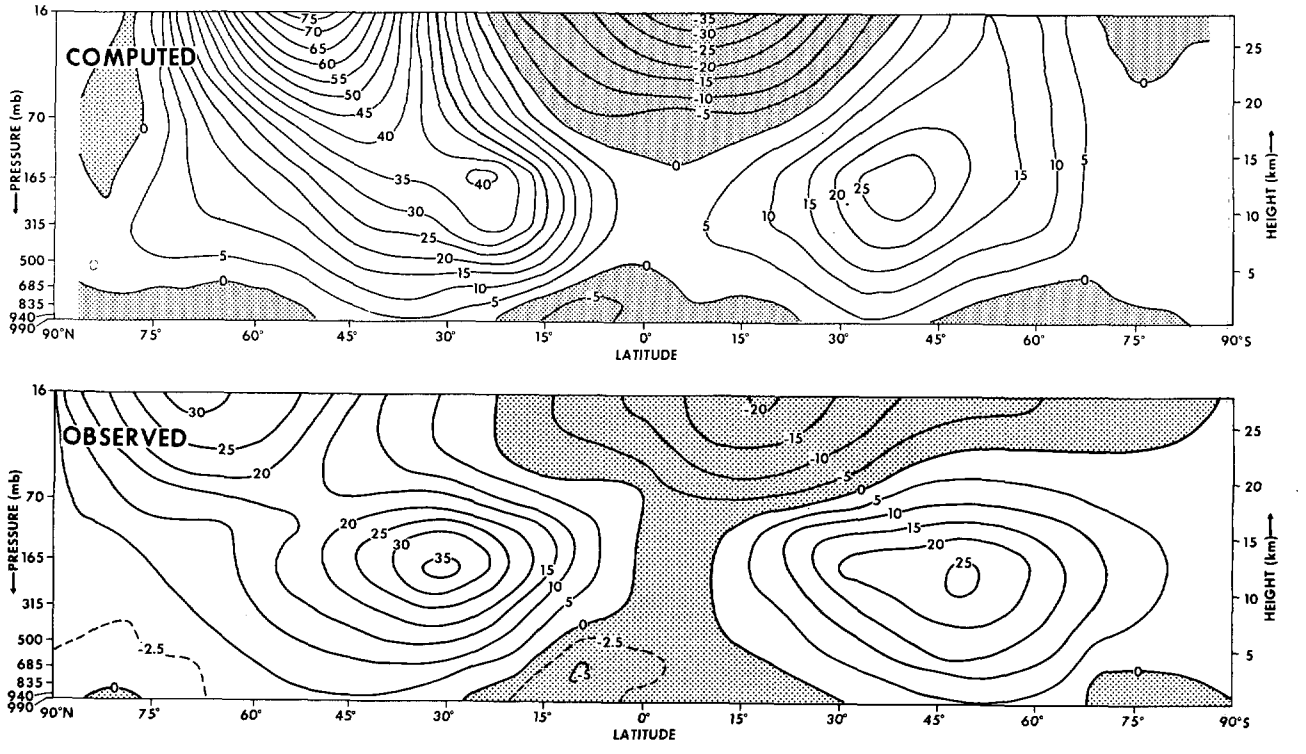

FIGURE 5.—Latitude-height distributions of the time-mean zonally averaged zonal component of the wind with easterly winds (negative values) shaded; units, m/s. The observed data are derived for December through February by Newell et al. (1969).

spheric jet streams in the model occur too close to the Equator by about 6° to 10° as compared with the observed jets in both hemispheres. However, their heights are about correct; and the maximum wind speeds of both jets are very well simulated by the model. The computed wind speeds in the stratospheric polar night jet and in the easterly wind belt in the tropical stratosphere are much too strong. Furthermore, the location of the polar night jet in the model is nearly 20° too far south.

Preliminary results from a time integration of an 11-level global model, incorporating a seasonal variation of solar radiation, show a markedly reduced intensity of the easterlies in the stratosphere of the model Tropics. Therefore, it is possible that the strong easterlies in the model stratosphere result from the assumption of a perpetual January or from the lack of a seasonal variation. The reason for the very strong jet in the winter stratosphere of the model is not clear to the authors.

Figure 6 shows the stream function of the mean meridional circulation computed from the time-mean meridional and vertical velocities given by the model. For comparison, on this same figure is shown the stream function of the Northern Hemisphere meridional circulation, computed by Oort and Rasmusson (1970) from observed winds for five Januaries (note that the streamlines in this figure are drawn at logarithmic intervals).

The Northern (or winter) Hemisphere Hadley cell is considerably larger and stronger than the corresponding direct cell in the Southern Hemisphere, and actually it straddles the Equator and crowds the weak Southern Hemisphere Hadley cell to the south. This asymmetry of the meridional circulation is caused by the asymmetries in the insolation and in the sea-surface temperatures. The intensities of the computed and observed northern Hadley circulations agree quite well, the centers being about 200×10^{12} g/s.

The strong northern Hadley circulation creates intense cross-equatorial flow at two levels [viz, a very shallow but strong boundary layer flow southward into the intertropical convergence zone (ITCZ), located at about latitude 10°S in the model, and a strong return flow just below the equatorial tropopause]. This meridional circulation in the Tropics supplies latent heat to the ITCZ at low levels and exports heat energy from the ITCZ in the upper troposphere. This subject is discussed in more detail in section 6. [See eq (39) for the definition of heat energy.] Manabe et al. (1970*b*) show that the heat of condensation is responsible for the remarkable intensity of the Hadley cell.

Agreement is also good for the locations and intensities of the Northern Hemisphere Ferrel and polar cells in the troposphere. The agreement between the two meridional circulations deteriorates toward the north, both because the model has certain deficiencies near the Poles (e.g., too high surface pressure) and because the observed stream function is least accurately estimated in the Arctic.

In the model stratosphere, a two-cell meridional circulation predominates; however, it is not evident in the stream function for the actual stratosphere shown in the lower

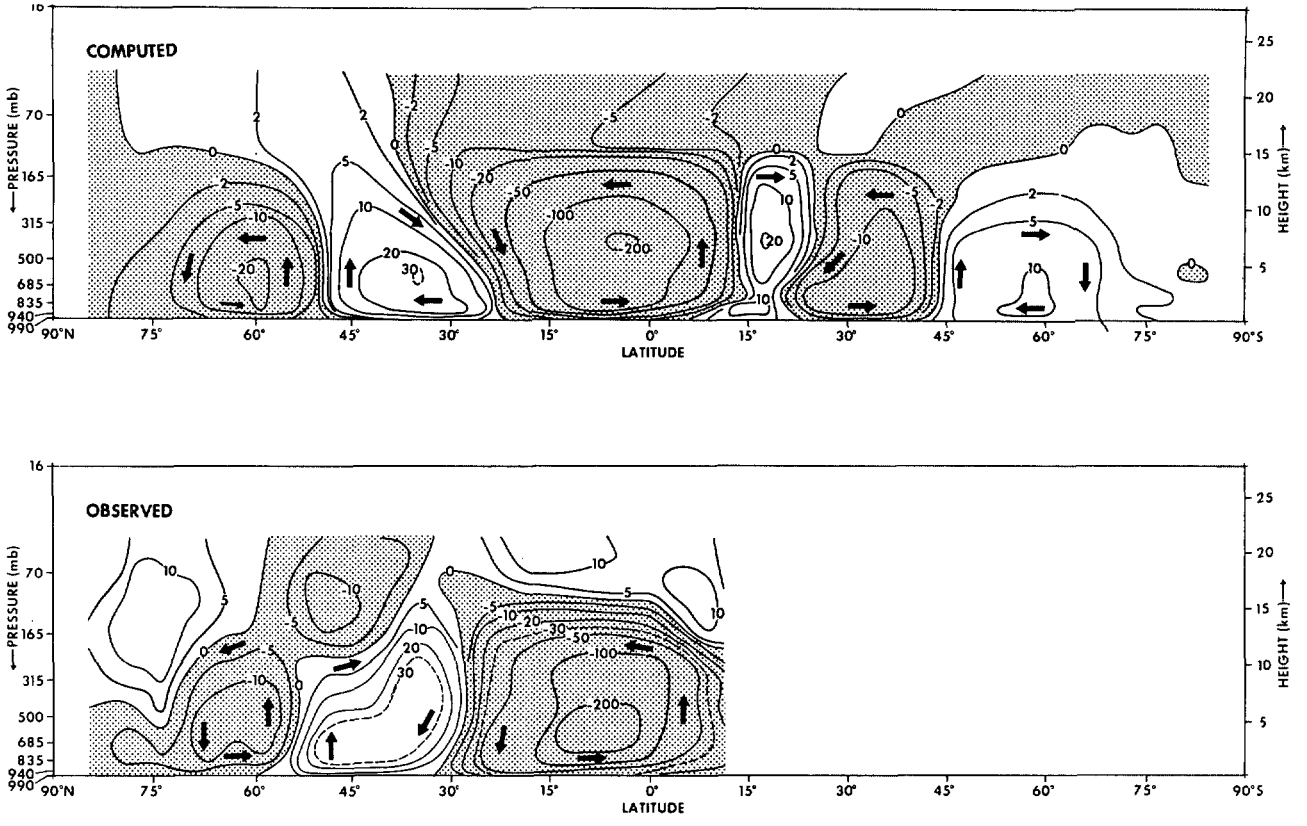

FIGURE 6.—Stream functions of the mean meridional circulation; units, 10^{12} g/s.

half of figure 6. One should note that the observed stream functions are least accurate in the stratosphere because of the inaccuracy of the wind measurements. Teweles (1965) and Miyakoda (1963) computed the distribution of vertical velocity by use of the so-called "adiabatic" method and by the ω equation, respectively. Both of their results clearly indicate a two-cell meridional circulation in the winter stratosphere.

C. SEA-LEVEL PRESSURE

The mean sea level pressure for the N24 model is plotted in figure 7 versus latitude and compared with the observed pressure curve derived for the Northern Hemisphere winter by Mintz (1968). The surface pressure over land is reduced to sea level by

$$p_{SL}=p_*\left[\frac{T_9}{T_9+\gamma z_*}\right]^{-g/R\gamma} \tag{38}$$

where p_{SL} is the sea-level pressure; T_9, the temperature of the lowest prognostic level; z_*, the height of the land surface above sea level; and γ, the lapse rate, assumed to be 6°K/km everywhere.

An unfortunate characteristic of the general circulation models used in this study is that they create much higher than normal sea-level pressures in polar regions (fig. 7). The mechanism producing these high polar pressures is probably a combination of several factors, some of which are unique to the type of grid system used for these models; two of these factors are:

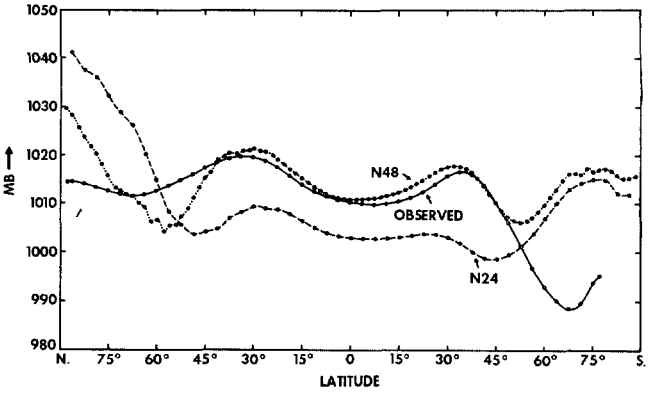

FIGURE 7.—Zonal mean sea level pressures observed in the actual atmosphere (solid line) and computed by the low resolution (N24) model (dashed line) and by the high resolution (N48) model (dotted line).

1. The assumption of a perpetual Northern Hemisphere winter insolation produces extreme cold over the polar region and excessive snow cover over the entire winter hemisphere. The resultant cold dome of air covering the north polar region favors the development of high pressure there.

2. As discussed in appendix A, subsection D, our models probably have a systematic bias in generating higher than normal pressures in polar regions.

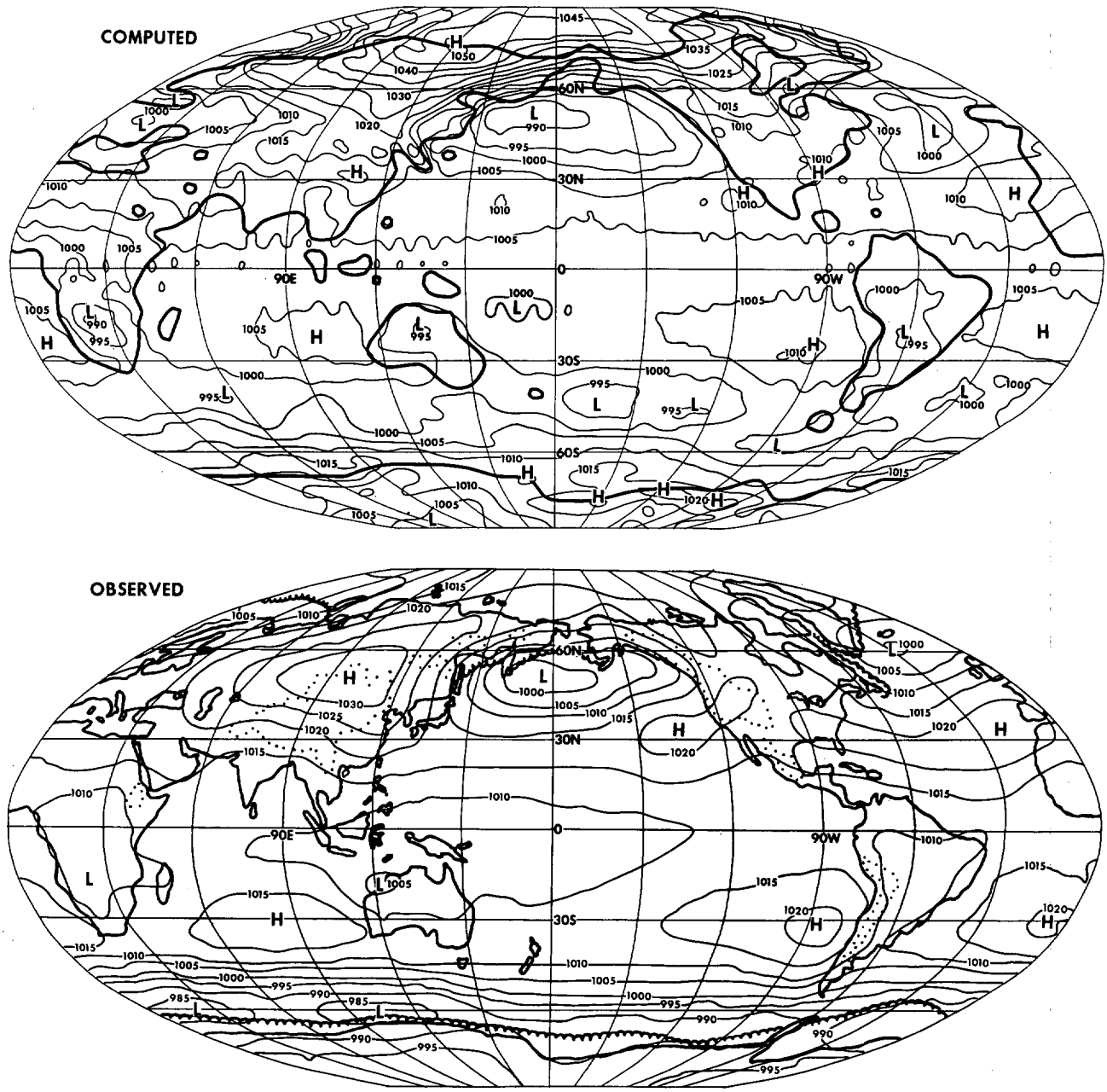

FIGURE 8.—Mean global sea-level pressure computed by the low resolution (N24) model and observed in the actual atmosphere; units, mb.

The computed meridional profile exhibits minima in the sea-level pressure in the Tropics and in the mid-latitude storm belts and high pressure at subtropical latitudes and in polar regions. However, these features of the computed distribution are shifted systematically toward the Equator from their counterparts in the observed profile. Furthermore, the intensities of the high-pressure belts in the model subtropics are too weak. Another failing of this model is the lack of a strong pressure gradient from latitudes 45° to 65°S which results in the model not properly simulating the location and strength of high-latitude surface westerlies in the Southern Hemisphere. The exact reasons for these unrealistic features of the model simulation are not determined; but they are partly related to the loss of computational accuracy, resulting from the coarseness and irregularities of the grid system mentioned above, as evidenced by the fact that a doubling of the resolution of the finite-difference grid greatly improves the zonal pressure distribution. In contrast to the low-resolution results, the mean zonal pressure of the high-resolution model exhibits a poleward shift of the pressure patterns, a reduction of the high polar pressures, and an intensification of the subtropical Highs and the middle latitude low-pressure belts (see appendix B for further details).

The two-dimensional global distribution of sea-level pressure is compared in figure 8 with the observed January mean global sea-level pressure compiled by Crutcher and Meserve (1970) in the Northern Hemisphere and by Tal-

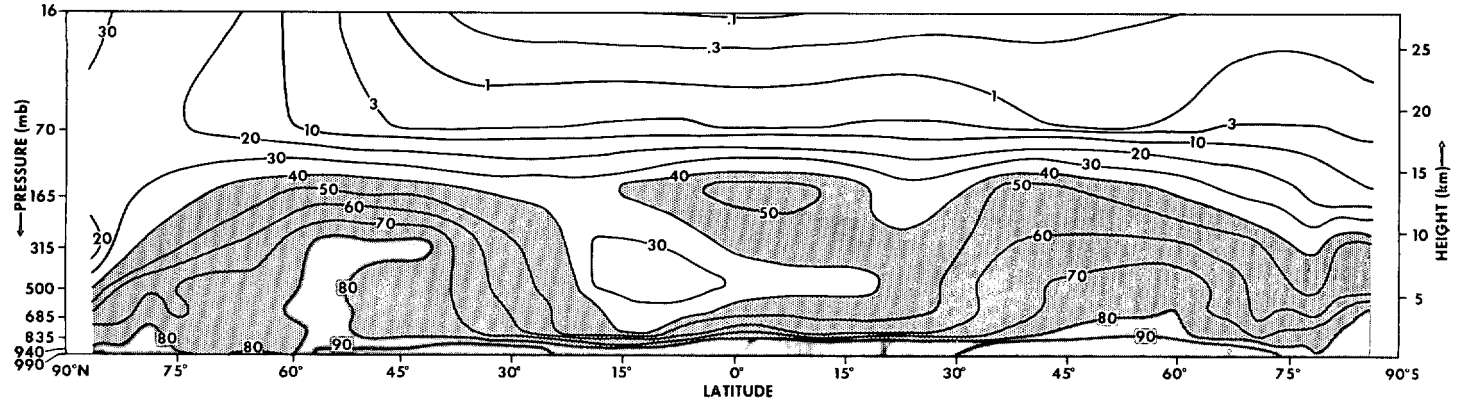

FIGURE 9.—Zonal mean latitude-height distribution of relative humidity from the low resolution (N24) model experiment. Relative humidities greater than 40 percent are shaded; those greater than 80 percent are indicated by darker shading.

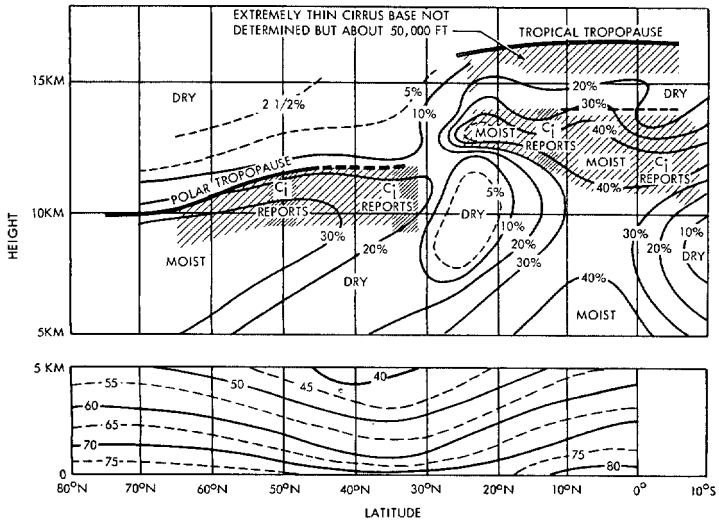

FIGURE 10.—Latitude-height distribution of the zonal mean observed relative humidity for the summer season based on data from Telegadas and London (1954) in the lower troposphere and Murgatroyd (1959) in the upper troposphere.

jaard et al. (1969) in the Southern Hemisphere. This map shows that, in the Northern Hemisphere, the model simulates a well-developed Aleutian Low but an underdeveloped Icelandic Low. On the computed pressure map, the Siberian High tends to merge into the highly exaggerated polar High. In the Southern Hemisphere, subtropical Highs form west of the three major continents (viz, Africa, Australia, and South America), in agreement with features of the observed distribution. However, the strengths of these Highs fail to attain climatic levels. Low-pressure centers develop over these Southern Hemisphere continents as a result of high surface temperatures (see subsection 3A). The low-pressure belt along the periphery of the Antarctic is simulated in the model experiment in qualitative agreement with observation, but it is not deep enough and is at too low a latitude. This feature of the Southern Hemisphere pressure distribution accounts for the lack of strong westerlies in high southern latitudes of the model experiment.

The distribution of sea-level pressure is markedly improved by the increase in resolution of the horizontal finite differences. For example, in the high-resolution model experiment, the strengths of subtropical Highs are enhanced significantly; and the Siberian High is clearly separated from the polar High because of the markedly decreased north polar pressures. See appendix B for details concerning this improvement.

D. HUMIDITY

The zonal mean latitude-height distribution of relative humidity from the low-resolution model experiment is presented in figure 9. The latitude-height distribution of mean observed relative humidity for the summer season is shown in figure 10, borrowed from the paper by Manabe et al. (1965). A comparison between these two figures shows that the mean computed relative humidity near the surface is too high at all latitudes compared with observation. In agreement with features of the actual atmosphere, the model stratosphere, in contrast, is very dry except at very high latitudes of the Northern (winter) Hemisphere. There are mid-latitude wet zones in both hemispheres. The dry zones in the subtropics, resulting from the descending motion in the poleward legs of the Hadley cells, seem to extend downward from the dry stratosphere aloft and spread into the mid-troposphere of the Tropics, in agreement with observed data. In the Tropics, the vertical motion is very strong in the mid-troposphere. The very dry air produced by this downward motion may be responsible for lowering the zonal mean relative humidity in the mid-troposphere.

In figure 11, the mean surface relative humidity computed by the model experiment is compared with the mean global distribution for January, derived by Száva-Kováts (1938). Over the oceans, the computed surface humidity exceeds the observed values by 10 to 20 percent. The reason for this is not obvious. However, realistically low

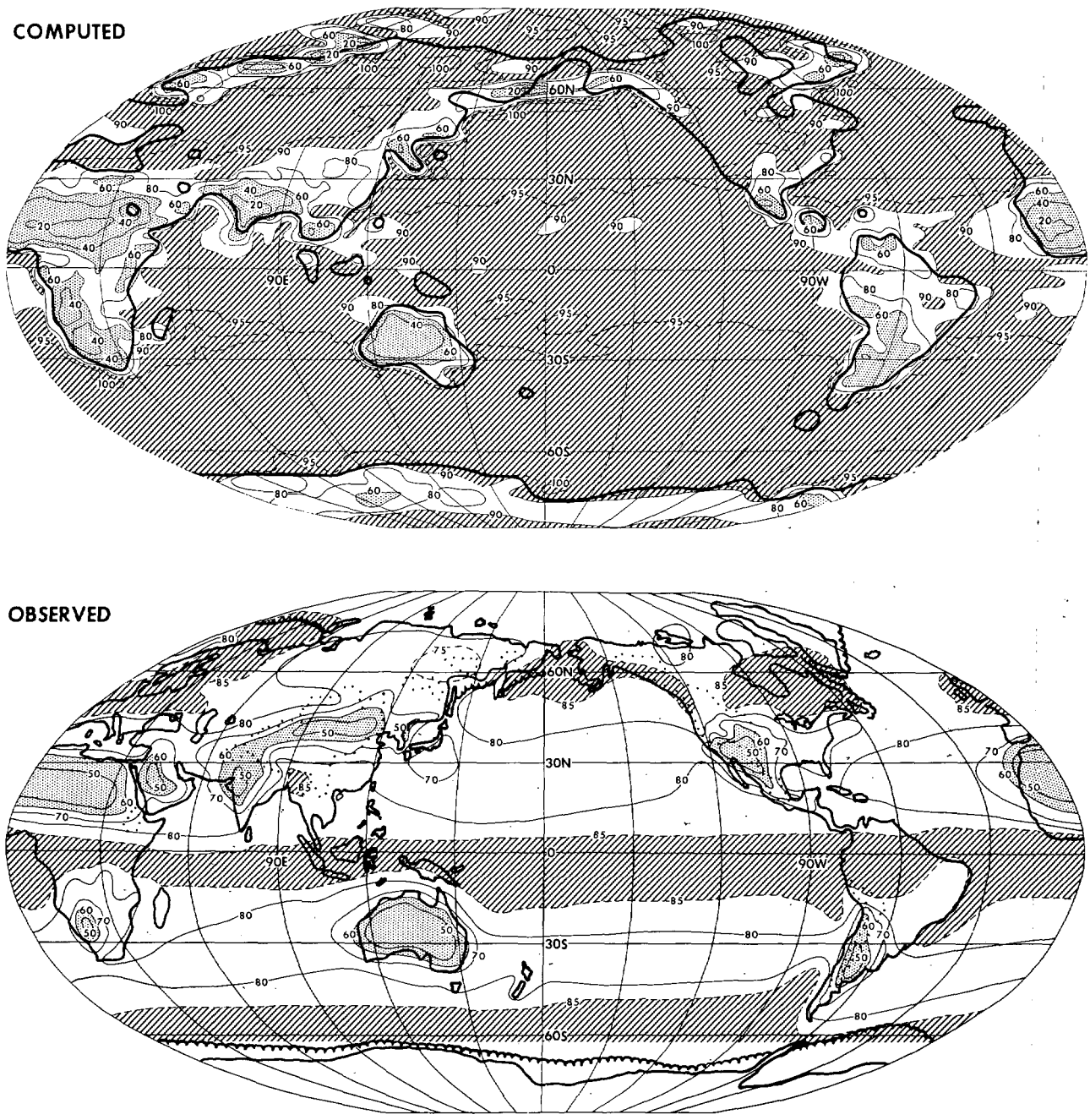

FIGURE 11.—Global mean relative humidities; areas of relative humidity below 60 percent are dotted; those above 90 percent are shaded by slashed lines on the computed map, and those above 85 percent are shaded on the observed map. Over the Antarctic, the observed data are missing.

values of relative humidity are correctly computed by the model for the arid regions of the world. For example, dry air is computed by the model near the ground over the Sahara, Australia, southwestern United States, and India during this season. Dry areas are also simulated in the southern parts of South America and South Africa, although in these areas the computed dry belts are somewhat too wide. As pointed out above, the surface temperatures of most of these dry regions are very high.

4. WATER BALANCE

In this section, we shall present global maps of the distributions of various hydrologic variables computed by the low resolution (N24) model experiment and compare these with climatic data.

Figure 12 shows a comparison between the computed mean precipitation rate and the observed rate derived from data for December, January, and February by Möller (1951). In this figure, areas with computed or observed

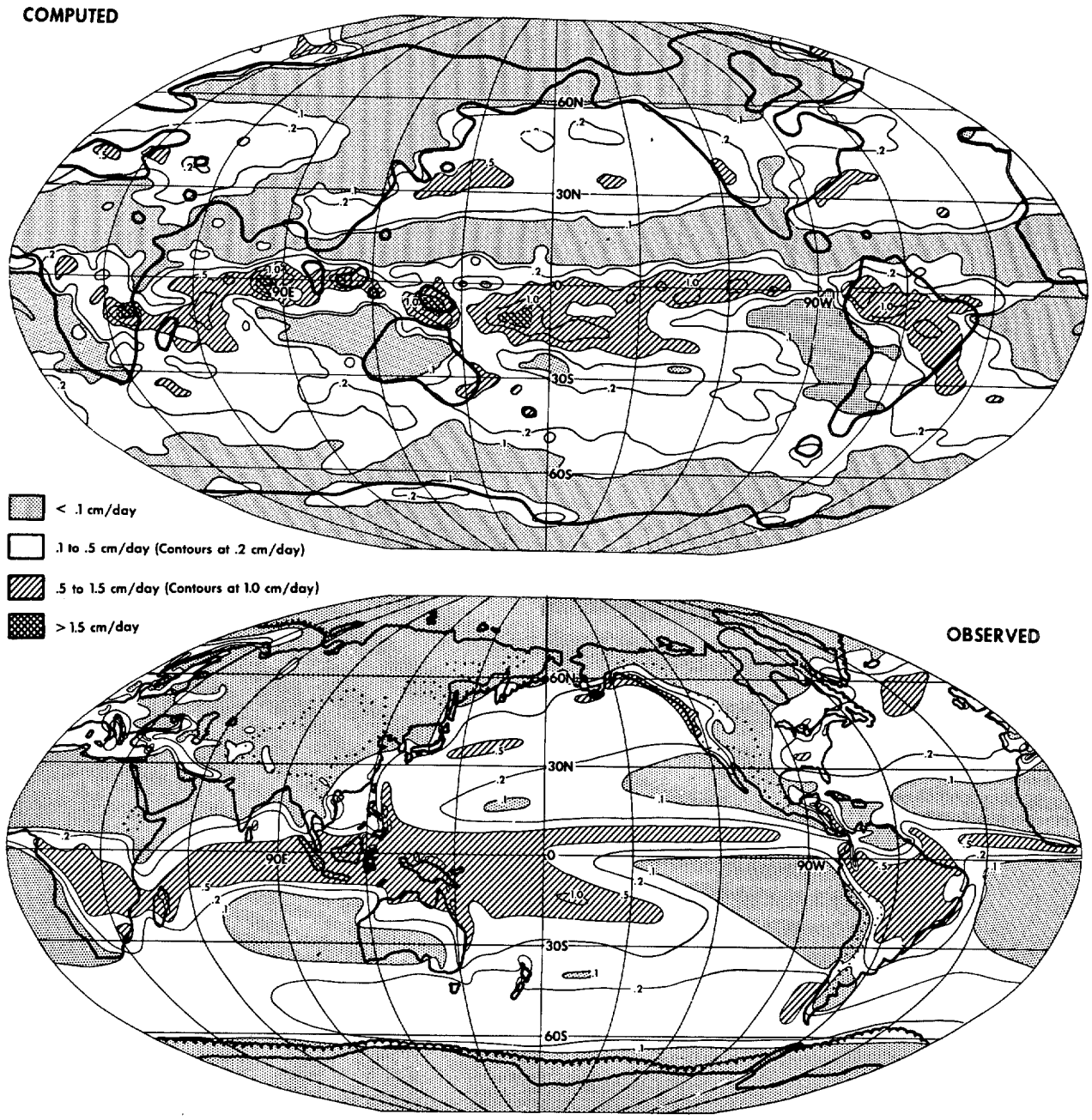

FIGURE 12.—Mean precipitation rate computed by the low resolution (N24) model compared with the estimated observed rate (Möller 1951).

precipitation rates in excess of 0.5 cm/day are shaded by diagonal lines, and dry regions with rates of precipitation lower than 0.1 cm/day are dotted. The computed distribution of precipitation exhibits a tropical rain belt, subtropical dry belts, middle-latitude moist regions, and polar dry zones that correspond rather well in location and intensity to the observed distributions.

From the eastern Indian Ocean eastward to the central Pacific Ocean, the computed tropical rain belt runs along the Equator or slightly to the south, in agreement with observation during this Northern Hemisphere winter season. This belt dips southward in the Amazon Valley in South America and toward Madagascar in the western Indian Ocean and swings northward in southern Africa, in good agreement with observed rainfall patterns.

The tropical rain belt splits into two legs in the eastern Pacific Ocean. The computed southern leg is not as well-developed as observed, and the northern leg straddles the Equator rather than being centered at about 5° to 10°N, as occurs in the real atmosphere. This latter discrepancy with observation can probably be attributed to the lack of a distinct minimum in the sea-surface temperature centered on the Equator, which occurs in nature but unfortunately is not very pronounced in the U.S. Hydro-

graphic Office (1944) data used for this model experiment. The cooler sea water actually observed at the Equator tends to suppress the genesis and development of tropical disturbances [e.g., see the results of the model experiment by Manabe and Bryan (1969)]. Thus, the observed rainfall maximum is shifted slightly northward to where the sea is warmer.

The location of the subtropical dry belt in the Southern Hemisphere in the model atmosphere agrees well with observation. The areas of minimum precipitation in this belt are off the west coasts of the continents where the oceanic anticyclones are located and the outflow from them predominates. The East Coasts are relatively wet, in agreement with the observed distribution of precipitation and with a similar model experiment by Manabe (1969). Dry air flowing out of subtropical anticyclones west of Africa and Australia causes the low precipitation rates and resulting deserts in the southwestern regions of these continents. The dry air flows more than halfway across Australia but is confined to the West Coast of South America. The reason for this difference is that, in South America, the very high Andes Mountain Range extending north-south along the entire continent just east of the West Coast effectively blocks the dry air from spreading eastward; but there are no such high and extensive mountains in the western part of Australia.

The precipitation patterns computed from a model without mountains confirm this theory by exhibiting a dry area across the entire southern part of South America. This phenomenon was discussed in Manabe and Holloway (1970*a*, 1970*b*). In fact, the computed distribution of precipitation given in figure 12 shows a greater eastward extension of the dry area in South America than is actually observed. As discussed in appendix C, this can be attributed to the smoothing of the model's topography that reduced the maximum height of the Andes far below the true elevations of these mountains. The Andes being rather narrow in the east-west direction are particularly susceptible to height reduction by space smoothing.

The Northern Hemisphere subtropical dry belt is well simulated by the model in location and magnitude of precipitation values. The extreme dryness of the Sahara Desert is well simulated by the model. The joining of the subtropical dry belt with the polar dry zone over North America is suggested but not completely realized by the N24 model results. However, in the precipitation distribution computed by the high resolution (N48) model, these two dry zones are joined in agreement with climatic data (see appendix B for further details).

The computed mid-latitude wet belt in the Southern Hemisphere is continuous around the entire globe, in agreement with observation, except in southern Argentina where the observed wet belt is slightly interrupted by the Andes. In the Northern Hemisphere, however, the wet zone in middle latitudes, computed by the model, is broken into cells by the mountains on the continents. This topographic effect is not as pronounced in the model as in nature because of the smoothness of the topography used in the model computations. The shallowness of the dry break in the middle of the North American Continent has been mentioned above. This northern middle-latitude moist belt is characterized by areas of high precipitation rate off the east coasts of the continents, in agreement with observation. The wet area, created off the northwestern coast of the United States, is centered too far south, which is no doubt related to the equatorward shift of surface-pressure patterns, as discussed in the previous section. Finally, for some unknown reason, precipitation rates over Europe are substantially above climatic values and those simulated by the high-resolution model run (see fig. 32 in appendix B).

In figure 13, the global distribution of evaporation rate computed by the model is compared with the evaporation rate distribution compiled by Budyko (1963). In the oceanic regions, the computed evaporation is significantly less than the rate estimated by Budyko, particularly in the subtropics. This discrepancy is, no doubt, related to the fact that the relative humidity is generally too high near the surface of the model oceans, as pointed out in the preceding section. Naturally, such high surface humidities tend to lower the general level of evaporation from the ocean surface. Although the rates of evaporation of the model have local maxima in the subtropical regions of both hemispheres in qualitative agreement with features of Budyko's distribution, the local maxima are too small and are located too close to the Equator. In the preceding section, it is pointed out that the oceanic anticyclones of the low resolution (N24) model are also located too close to the Equator. Since the oceanic anticyclones produce outflow of very dry air over the ocean surface, they tend to enhance evaporation. Accordingly, the discrepancy between the observed and computed locations of the subtropical anticyclones seems to be partially responsible for the unrealistic distribution of evaporation mentioned above. In middle latitudes, evaporation from the oceanic surfaces of the model is most rapid off the east coasts of the Eurasian and the North American Continents, in excellent agreement with features of Budyko's distribution. In these areas, cold continental air with low absolute humidity flows out over the warm oceanic surfaces, which creates large air-sea temperature differences and enhances evaporation.

In continental regions, agreement between the model's distribution and Budyko's is better. For example, the model computes a very low rate of evaporation in deserts such as the Sahara, southwestern Africa, and southern South America, in good agreement with Budyko's distribution. In high northern latitudes and in the Antarctic, the evaporation rate of the model is very small. In fact, in a few northern latitude areas, the evaporation rate is even slightly negative, which indicates frost formation. The effective reflection of solar radiation by snow or pack ice leaves little energy available for sublimation in these areas.

421-361 O—71——2

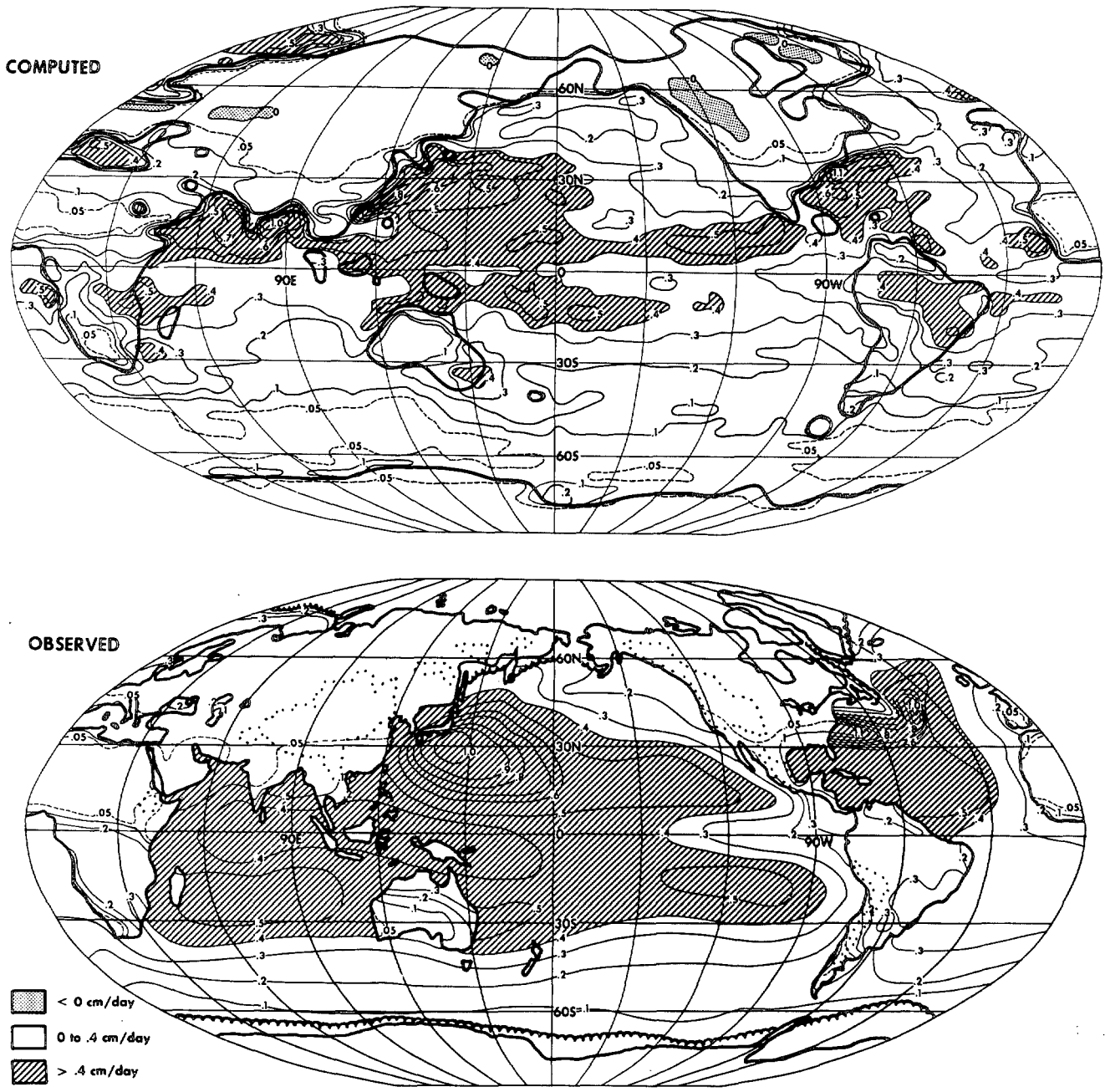

FIGURE 13.—Global distribution of evaporation rate computed by the N24 resolution model and the same rate derived by Budyko (1963) from observed data.

Figure 14 depicts the computed soil moisture on the model continents. Dry areas having less than 0.5 cm of soil moisture are dotted; and wet regions, where the soil moisture is greater than 5 cm in depth, are indicated by slashed shading. The snowline, shown as a dashed line, appears too far south on all Northern Hemisphere continents because of perpetual winter. The arid regions of the earth, having little soil moisture, are well simulated by the model. For example, the Sahara, the desert in Western Australia, and the arid region of southwestern Africa are well represented by the computed soil moisture distribution. These are areas of little precipitation as observed in nature and as simulated by the model (fig. 12). On figure 14, India appears as a desert. Recall, however, that the season of this model experiment is a perpetual January, which is the time of the winter monsoon in India when there is little or no rain in this country. If this experiment had incorporated a seasonal variation of insolation, rainfall would have occurred in India during the summer season, and desert conditions would not have become established here. The desert area of the southwestern United States is shifted southward into Mexico. This is certainly related to the extensive snow cover to the north as well as to the equatorward shift of pressure patterns,

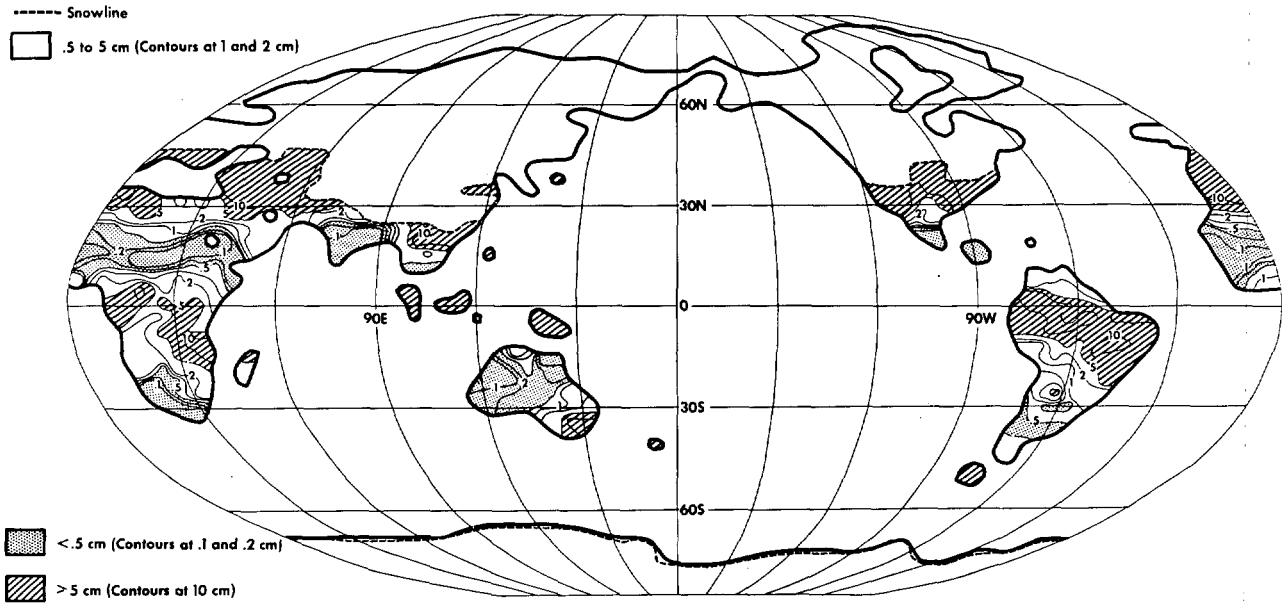

FIGURE 14.—Computed soil moisture on the N24 resolution model continents.

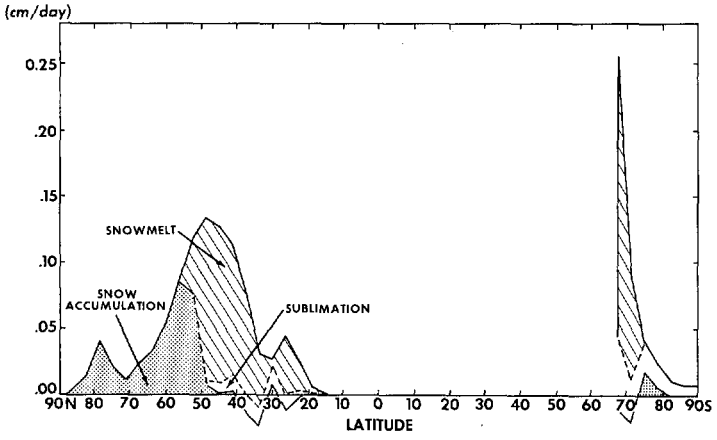

FIGURE 15.—Zonal mean distributions of various snow balance components. The envelope of curves is the snowfall rate; subtracting from this is the snowmelt rate (shaded by slashed lines). The sublimation rate is subtracted from the remainder but is left unshaded. The net snow accumulation rate is dotted.

discussed in the previous section. The computed areas of deep soil moisture amounts coincide with regions of tropical rain forests (viz, tropical Africa, the Amazon River Basin, and the Indonesian Islands).

Large areas of the continents of the Northern Hemisphere of the model are snow covered. Figure 15, which shows the zonal mean distributions of various snow balance components on the continents, indicates that snow accumulates significantly north of 45°N with a maximum around 55°N. As pointed out, the extensive accumulation of snow cover results chiefly from the assumption of a perpetual January insolation. In view of the lack of a seasonal variation in the model insolation, we felt that the distribution of soil moisture beneath the snow cover is not meaningful. Therefore, it is not shown in figure 14. According to figure 15, the latitude of the maximum rate of snowfall does not coincide with the latitude of the maximum rate of snow accumulation because of the effect of snowmelt. In the Northern Hemisphere, the rate of snowmelt is at a maximum around 45°N; and in the Southern Hemisphere, it is at a maximum at the periphery of the Antarctic Continent. As will be indicated in the following paragraph, the snowmelt contributes very significantly to the runoff in the Northern Hemisphere of the model.

Figure 16 depicts the distribution of runoff computed on the model continents. White areas indicate no runoff, and slashed shading indicates regions with runoff greater than 0.1 cm/day. For the most part, these areas correspond well with the watersheds of some of the earth's major rivers (e.g., the Amazon in South America; the Congo, the Zambezi, and the source of the Nile in Africa; and the rivers in eastern and western United States). According to the comparison between the distribution of runoff rate and that of snowmelt rate shown in figure 17, the areas of major runoff in the Northern Hemisphere of the model correspond very well with those of snowmelt, indicating the significant contribution of snowmelt to runoff in these areas. This comparison also indicates that the excessive runoff in the western part of the Eurasian Continent results mainly from the excessive snowmelt taking place there. This snowmelt occurred during the early part of the averaging period and is responsible for a rapid decrease in snow depth there.

Evaporation from the earth's surface represents a source of water vapor in the atmosphere, and precipitation, on the other hand, is a sink for atmospheric water. The distributions of these two meteorological phenonema point out the locations of major sources and sinks of

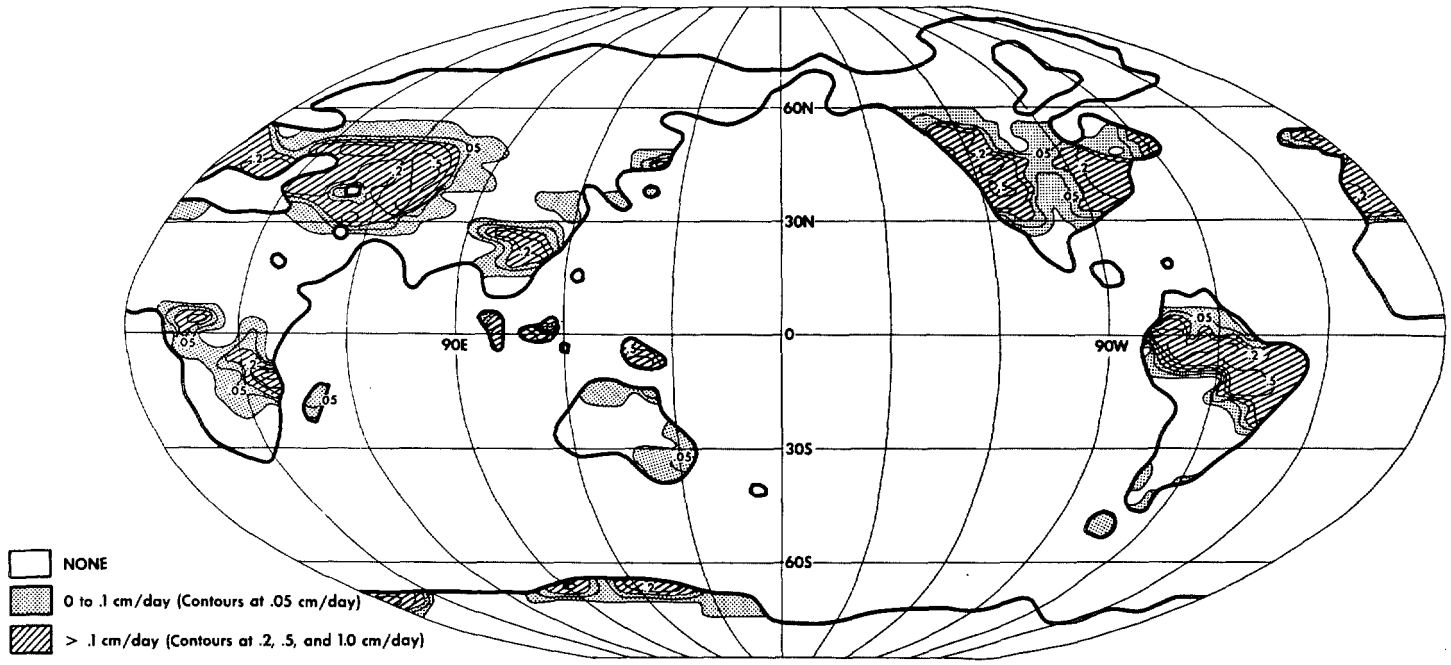

FIGURE 16.—Distribution of runoff computed for the model continents.

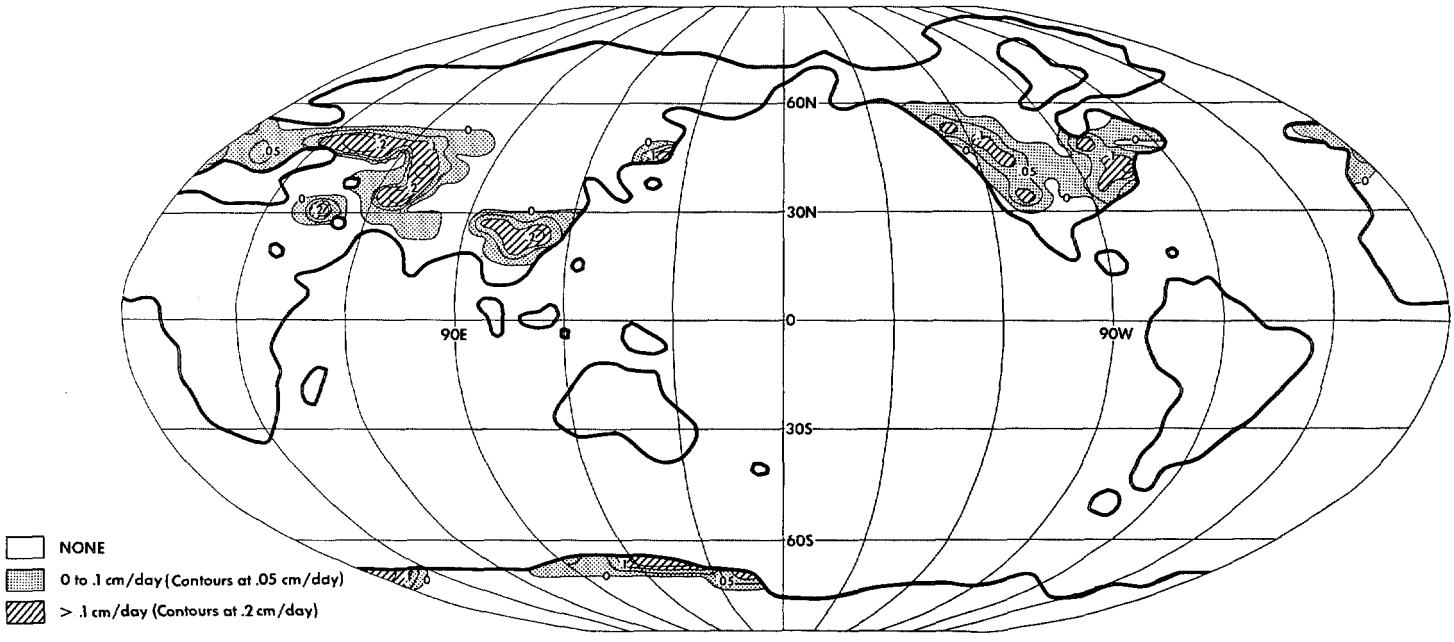

FIGURE 17.—Computed global distribution of mean snowmelt rate during the 70-day period of averaging of the N24 model experiment.

atmospheric water vapor. Figure 18 shows the model's zonally averaged evaporation and precipitation for the whole earth, continental areas, and oceans as a function of latitude. This figure shows that the major source of water vapor is over the subtropical oceans of the Northern (or winter) Hemisphere where precipitation is suppressed by the general downward motion and the evaporation from the earth's surface is enhanced by high sea-surface temperatures. The major sink of atmospheric water vapor is in the ITCZ, especially over land where orography enhances the already intense tropical precipitation rates. Secondary sinks are evident in middle-latitude rain belts, particularly in the continental region of the Northern Hemisphere.

At points where the curves for precipitation and evaporation diverge are areas of deficiencies or excesses of moisture that must be compensated by transport from other areas. For example, the net excess of water vapor

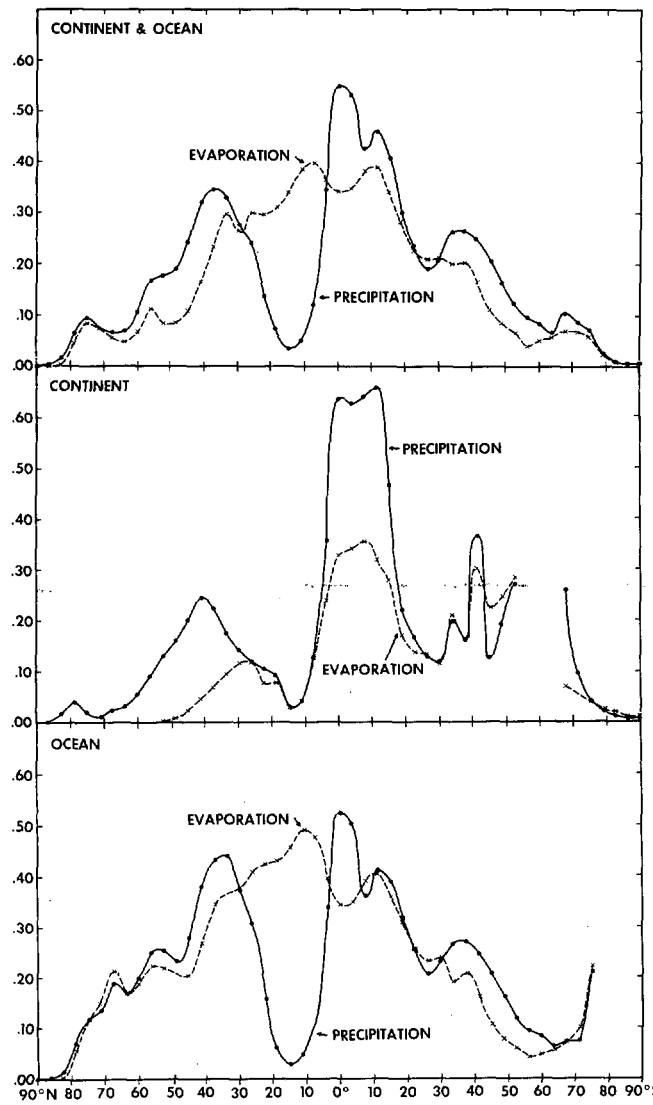

FIGURE 18.—Latitudinal distributions of the rates of precipitation and evaporation (in cm/day).

added to the atmosphere in the northern oceanic subtropics must be transported to the Tropics or to the mid-latitude storm belt where precipitation exceeds evaporation. On the other hand, subtropical continental areas have low values of both evaporation and precipitation so that net advection of water vapor into or out of these areas is very small. The resultant transport of latent energy by the advection of water vapor in the model atmosphere is discussed in section 6.

5. HEAT BALANCE

A. HEAT BALANCE OF THE EARTH-ATMOSPHERE SYSTEM

The heat balance of the earth-atmosphere system is determined by the net radiative flux at the top of the atmosphere. In table 2, the global mean values of radiative fluxes of the model atmosphere are compared with those

TABLE 2.—*Fluxes of radiation at the top of the atmosphere (in* ly/min)

Kind of radiation	vonder Haar Dec., Jan., Feb.	Model Jan.
Incident solar	0.51	0.51
Net downward solar	.35	.32
Net upward terrestrial	.32	.30

of the actual atmosphere estimated by vonder Haar (1969) for the period from December to February. It should be pointed out that the results of vonder Haar are based on recent observations from meteorological satellites. This table indicates that both the net downward flux of solar radiation and the net upward flux of longwave radiation at the top of the model atmosphere are significantly less than those at the top of the actual atmosphere, as estimated by vonder Haar. The difference in the magnitude of the net solar radiation is chiefly due to the difference in planetary albedo between the model and the actual atmosphere. According to our computation, the planetary albedo of the model atmosphere is approximately 0.37, which is larger than the albedo of the actual atmosphere, as observed from meteorological satellites (0.31). One of the reasons for this discrepancy is the excessive snow cover of high reflectivity in the Northern Hemisphere of the model, which has been mentioned in preceding sections. However, there may be other reasons for this discrepancy. As vonder Haar indicated, the planetary albedo obtained from satellite observations is approximately 5 percent less than the theoretical estimate by London (1957). Since the distribution of clouds and their optical properties (used in this study) are very similar to those adopted by London, it is probable that our cloud properties suffer from the same deficiencies as London's and thus may also be significantly different from reality.

Fortunately, an error in the planetary albedo may not result in an extremely unrealistic climate in this study because the distribution of sea-surface temperature is specified as a lower boundary condition. However, a several percent difference in planetary albedo may markedly alter the climate of a joint ocean-atmosphere model in which the sea-surface temperature is determined as the results of the interaction between the oceanic and the atmospheric parts of the model (see Manabe and Bryan 1969). Therefore, it seems to be very important to identify the causes of this discrepancy by repeating the heat balance study of London with the improved data.

The latitudinal distributions of the zonal mean values of the net radiation fluxes at the top of the model atmosphere are shown in figure 19. For comparison, the corresponding quantities estimated by vonder Haar (1969) for the actual atmosphere are also plotted in this same figure. As pointed out, fluxes of both solar and terrestrial radiation of the model are significantly less than the

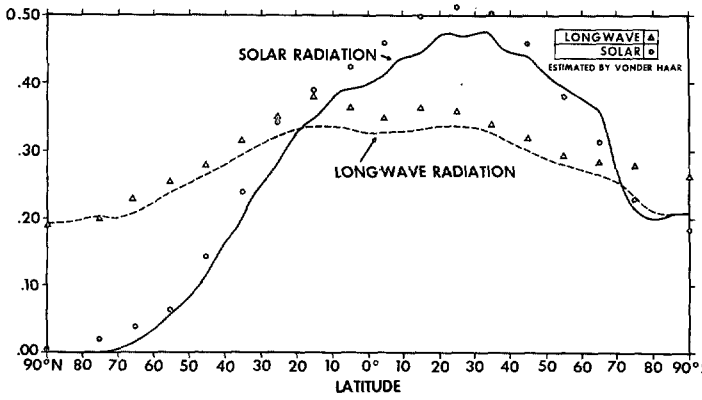

FIGURE 19.—Latitudinal distributions of the zonal mean values of the net downward solar radiation and the upward longwave radiation at the top of the model atmosphere (in ly/min).

observed values, particularly at low latitudes where London's cloud distributions may be inaccurate. Careful re-examination of the cloud distribution by means of satellite data are highly desirable. The general features of the model distribution, however, agree well with the observed distribution.

For depicting the horizontal distribution of the radiative imbalance, the global distribution of the flux of net downward radiation at the top of the model atmosphere is shown in the upper half of figure 20. The distribution of the corresponding quantity in the actual atmosphere, as estimated by vonder Haar (1969) from satellites, is added for comparison to the lower half of this figure. The general features of the two distributions agree well with each other, although the model distribution lacks some of the longitudinal variations in the net flux, which are

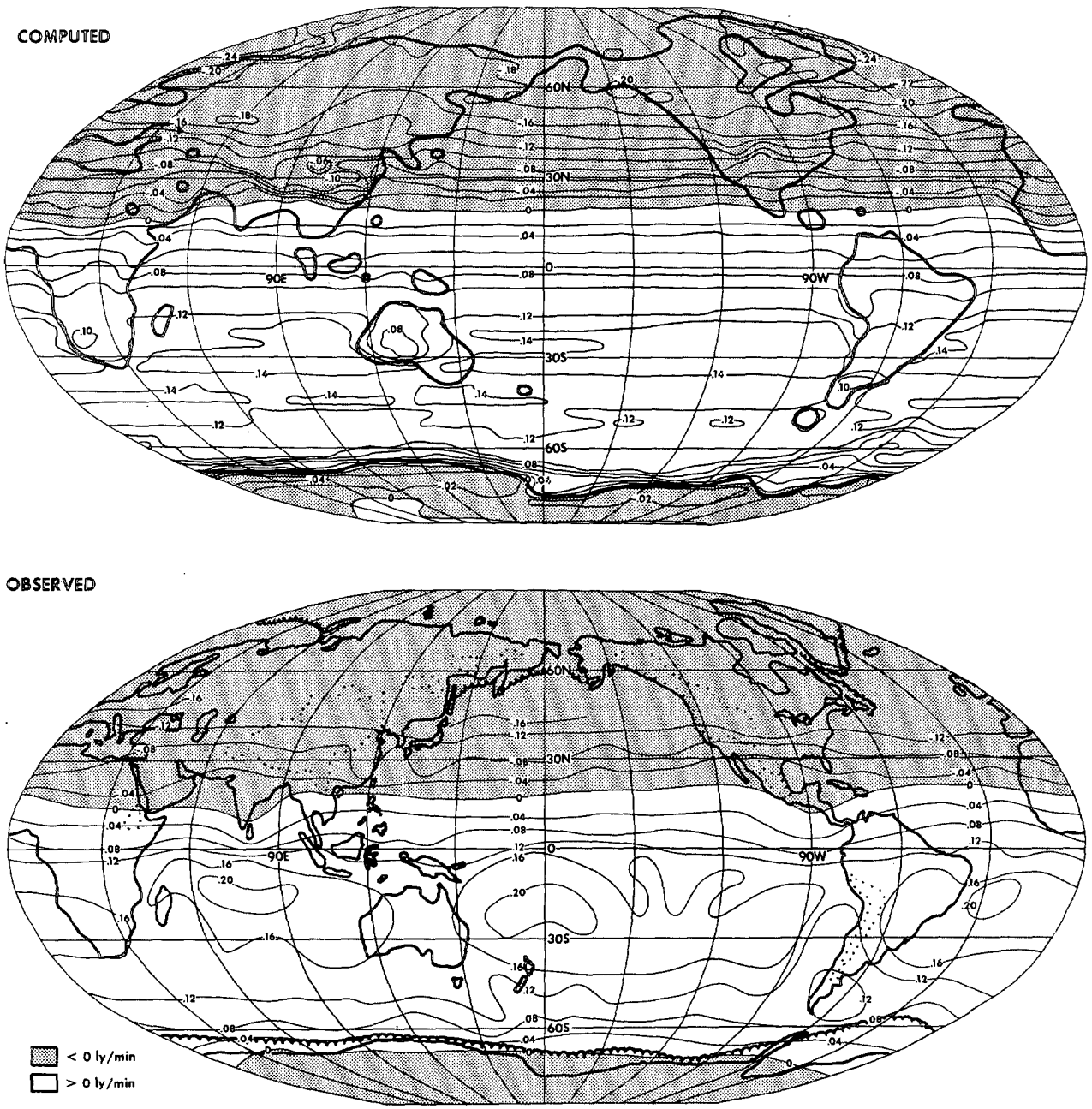

FIGURE 20.—Global distribution of the flux of downward radiation [= (net downward solar radiation) − (net upward terrestrial radiation)] at the top of the atmosphere.

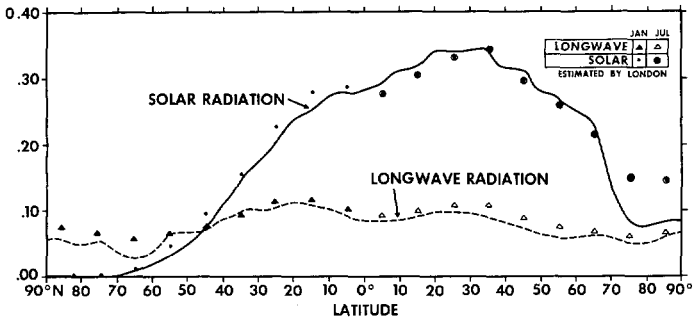

FIGURE 21.—Latitudinal distribution of the zonal mean values of the net downward solar radiation and the net upward longwave radiation at the surface of the model earth (in ly/min).

evident in the vonder Haar distribution (note that the cloud distribution assumed for the computation of radiative transfer lacks a longitudinal variation). The net flux of the model is, nevertheless, significantly smaller than the observed flux at low latitudes, particularly in the subtropics of the Southern Hemisphere, as pointed out in the preceding paragraph.

B. HEAT BALANCE OF THE EARTH'S SURFACE

The heat fluxes contributing to the heat balance at the surface of the model earth are the fluxes of solar and terrestrial radiation, the turbulent fluxes of sensible and latent heat into the atmosphere, and the heat flux to the interior of the ocean. In this subsection, we shall examine the distribution of these fluxes. According to figure 21 showing the latitudinal distribution of the radiative fluxes at the surface of the model earth, the net downward flux of solar radiation is much larger than the net upward flux of terrestrial radiation except at high latitudes of the Northern Hemisphere where the flux of solar radiation is very small. The corresponding quantities at the surface of the actual earth in the Northern Hemisphere, estimated by London (1957), are also plotted for comparison in this figure where July Northern Hemisphere values are used for the Southern Hemisphere summer (January). The agreement between the radiation fluxes computed by the model and those estimated by London from observed data appear, in general, to be very close.

Figure 22 is presented to show how the heat gain resulting from the net downward flux of radiation [=(downward flux of solar radiation)−(upward flux of longwave radiation)] is compensated by the other heat balance components mentioned above. The distributions on the continents and those on the oceans are shown separately for detailed examination.

On the model continents, because of the assumption of a zero heat capacity of the ground surface, the heat gain from the net downward radiation is exactly compensated by the heat loss, which is due to the upward fluxes of sensible and latent heat. In the Tropics and in middle latitudes of the model where soil moisture is relatively large as a result of the excess of precipitation over evaporation, the latent heat flux is chiefly responsible for removing heat

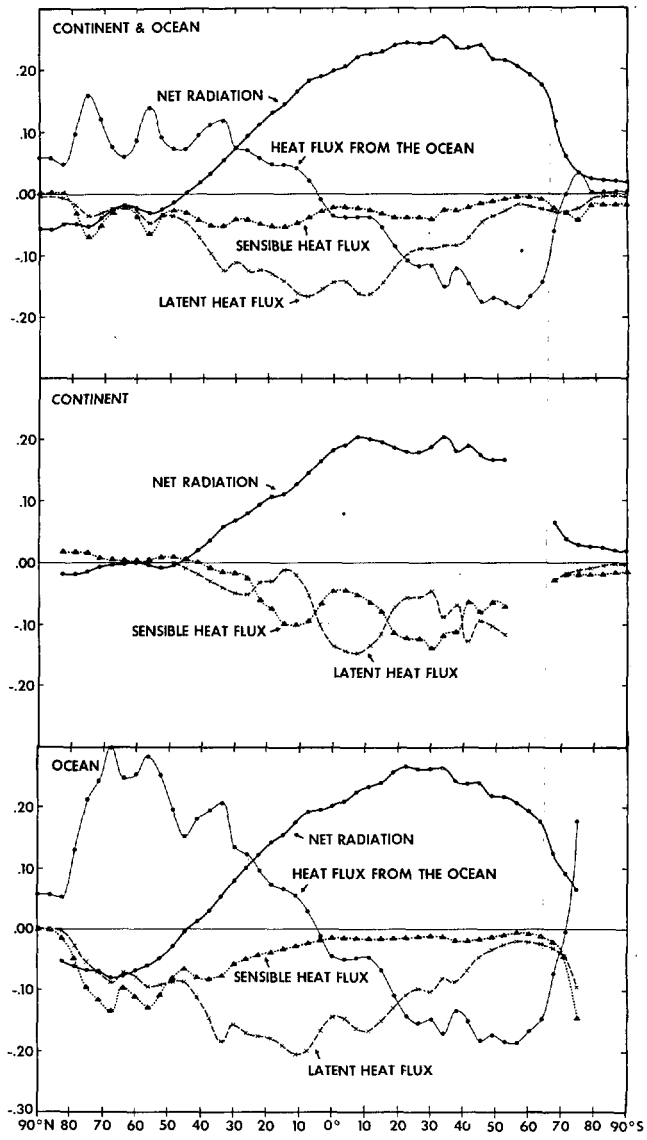

FIGURE 22.—Latitudinal distributions of the zonal mean values of various heat balance components at the surface of the model earth (in ly/min). Thin solid line indicates the heat flux from the interior to the surface of the ocean.

from the ground surface. On the other hand, sensible heat flux plays a major role in the removal of heat from the ground surface of the model subtropics where soil moisture is small because of meager precipitation. In short, sensible and latent heat fluxes supplement each other in removing heat from the ground surface of the model.

Over the model oceans, the sensible heat flux is much smaller than the latent heat flux except at very high latitudes. In general, the Bowen ratio, which is the ratio of sensible heat flux to latent heat flux, increases with increasing latitude, in agreement with the features of the energy exchange over the actual oceans. Over ocean surfaces (different from the case of a land surface), the heat loss due to both sensible and latent heat fluxes does not necessarily compensate for the heat gained by net downward radiation. The imbalance among these components constitutes the heat sources and sinks for the model oceans. As figure 22 indicates, the model oceans gain heat in the Southern

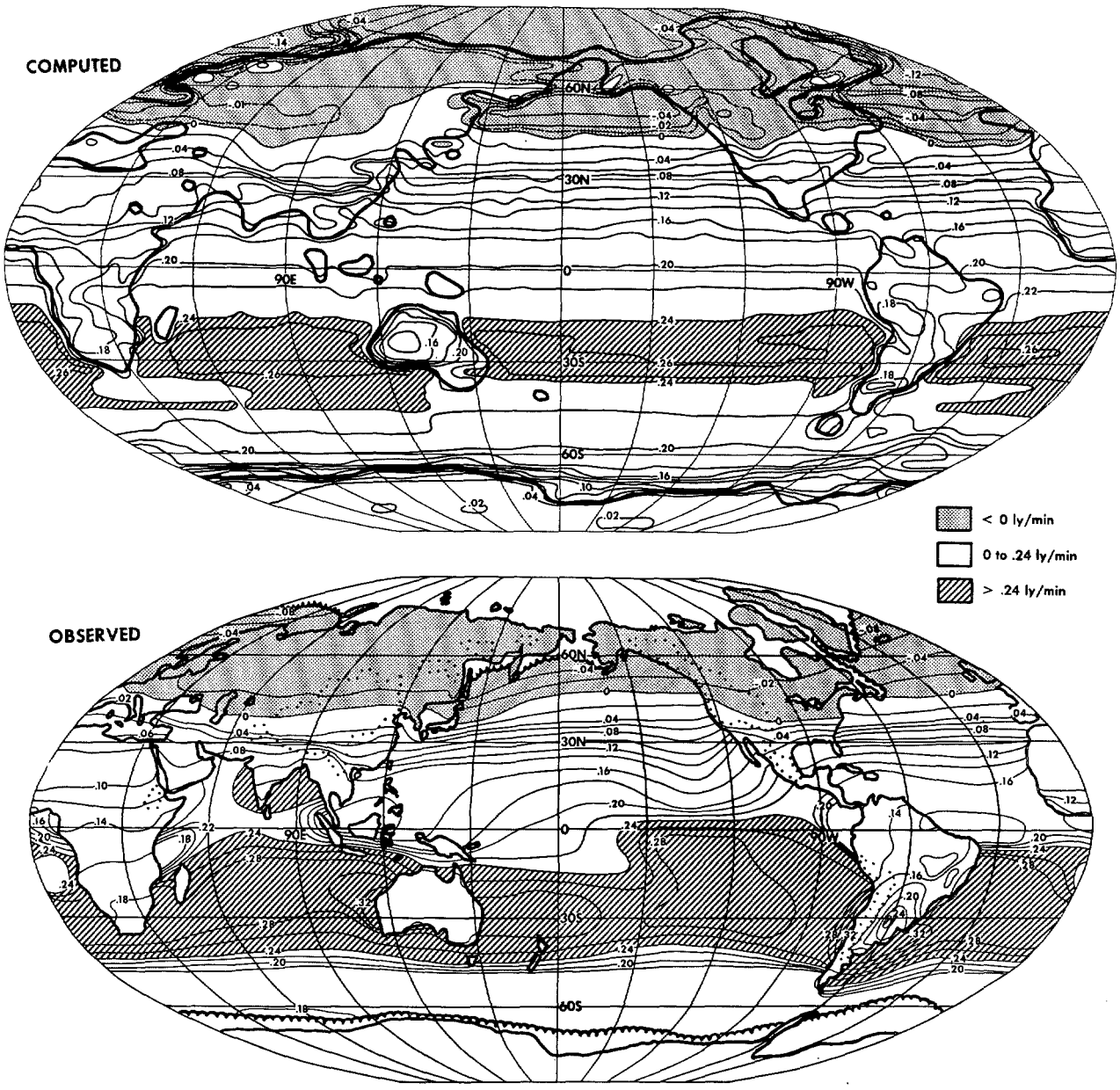

FIGURE 23.—Global distribution of net downward radiation at the earth's surface. The net downward radiation is defined as the difference between the net downward solar radiation and the net upward longwave radiation.

(summer) Hemisphere and lose heat in the Northern (winter) Hemisphere.

Thus far, we have discussed the latitudinal distributions of various heat balance components at the earth's surface. Next, we shall briefly describe the global distributions of these components. The global distributions of net downward flux of radiation and of net upward flux of sensible heat at the surface of the model earth are shown in the upper halves of figures 23 and 24, respectively. The distributions of the corresponding quantities at the surface of the actual earth, estimated by Budyko (1963), are added to the lower halves of these figures for comparison. Another heat balance component (i.e., latent heat flux at the surface of the model earth) may be inferred from figure 13 which shows the global distribution of the evaporation rate.

According to figure 23, the general features of the distributions of the net downward flux of radiation at the surface of the model earth are quite similar to those of Budyko's distribution. For example, the net downward radiational flux of the model is maximum in the subtropics of the Southern Hemisphere except over the continents where the net downward flux is very small because of the high temperatures of the ground surface. This flux is negative in high latitudes of the Northern Hemisphere, in agreement with the same features of Budyko's distribution. On the other hand, there are significant differences between

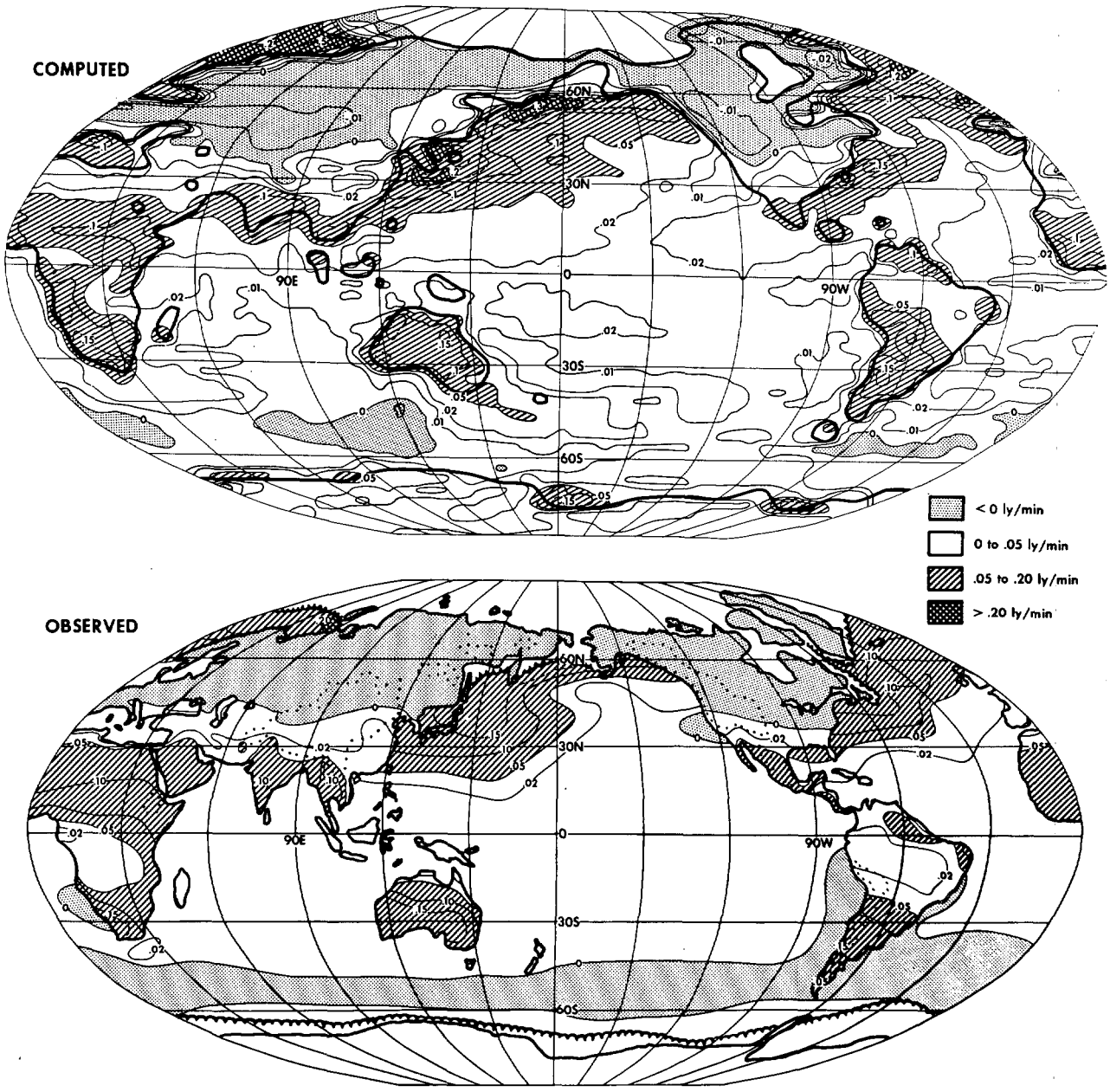

FIGURE 24.—Global distribution of net upward flux of sensible heat at the earth's surface.

the two flux distributions. In general, the net downward radiation flux of the model has a more zonal distribution than the flux of the actual atmosphere, probably a result of the lack of a zonal variation in cloudiness. Furthermore, the net flux of the model is significantly less than the flux estimated by Budyko in the subtropics of the Southern Hemisphere. Again, it is highly probable that the inaccurracy of cloudiness in the model is responsible for this discrepancy. Statistical studies of cloud data obtained from meteorological satellites are required to verify these speculations.

In general, the distribution of the sensible heat flux of the model (upper half of fig. 24) is much less zonal than that of the net downward radiation. In the Southern (summer) Hemisphere and in the lower latitudes of the Northern Hemisphere, the sensible heat flux of the model is relatively large over the continents, particularly over arid regions such as the Sahara Desert, the Australian Desert, Mexico, and India. In these areas, the magnitude of the latent heat flux is small because of insufficient soil moisture; and a large amount of sensible heat flux is required to compensate for the large values of net downward radiation. Over the continents in middle and high latitudes of the Northern Hemisphere, the sensible heat flux of the model has a small negative value as a result of the temperature inversion at these latitudes. Since most

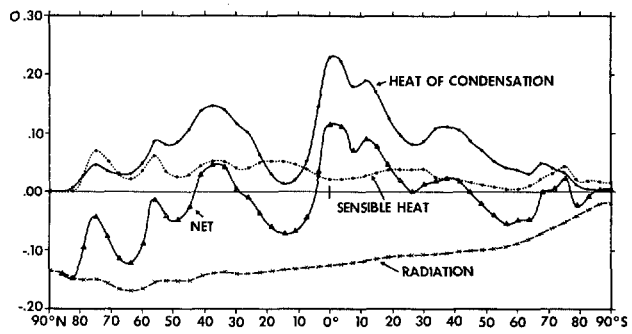

FIGURE 25.—Latitudinal distributions of the zonal mean values of various heat balance components in the atmosphere (in ly/min).

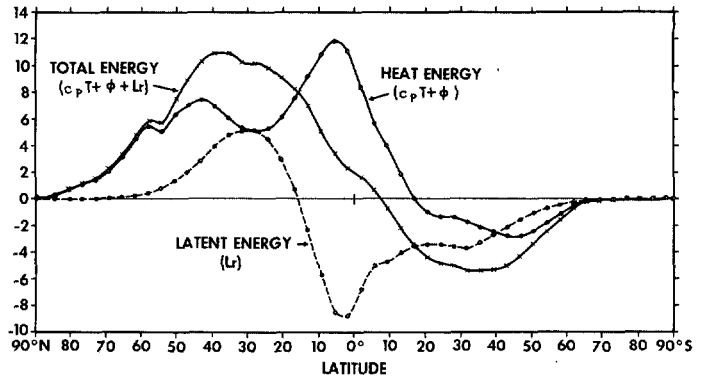

FIGURE 26.—Latitudinal distributions of the northward transport of energy ($\times 10^{19}$ cal/day).

of the weak insolation reaching the surface here is reflected by snow cover, the magnitudes of all heat balance components are very small over the model continents. Over the oceanic regions of the Northern Hemisphere, the sensible heat flux of the model is very large off the east coasts of the continents where the outflow of cold continental air over warm ocean currents takes place. These features of the model distributions are in excellent agreement with those of Budyko's distribution shown in the lower half of figure 24. This agreement suggests that the computation schemes for the heat and water balance at the continental surfaces of the model are working properly, despite the extreme idealization of the various processes involved.

C. HEAT BALANCE OF THE MODEL ATMOSPHERE

The components of the heat balance in the atmosphere are the net radiation, the heat of condensation, and the supply of sensible heat from the earth's surface to the atmosphere. Figure 25 shows the latitudinal distributions of the zonal mean values of these heat balance components in the model atmosphere. According to this figure, radiation has a cooling effect at all latitudes of the model; and the other two components of the heat balance already mentioned have a heating effect and tend to compensate for the radiative cooling. The imbalance among the three components is indicated by a solid line identified as "net." In the model atmosphere, large values of net heating occur in the Tropics of the Southern Hemisphere where the heat of condensation released by the tropical rain belt is very large. On the other hand, a great deal of net cooling takes place in the subtropics of the Northern Hemisphere and in high latitudes where the heat of condensation is practically negligible. The latitudinal distribution of the heat imbalance described here is such that the cells of meridional circulation are intensified, particularly the cross-equatorial Hadley cell, as discussed in subsection 3B.

6. MERIDIONAL ENERGY TRANSPORT

The latitudinal distributions of the imbalances in the water vapor and heat budgets in the model atmosphere, described in sections 4 and 5 should be compensated by the meridional transports of water vapor and heat energy by the atmospheric circulation. Figure 26 shows the distributions of the northward transports of heat energy, latent energy, and total energy required for compensating the imbalance in the heat and water vapor budgets of the model atmosphere. In this paper, heat energy, latent energy, and total energy are defined as

$$(\text{heat energy}) = c_pT + \phi, \tag{39}$$

$$(\text{latent energy}) = Lr, \tag{40}$$

and

$$(\text{total energy}) = c_pT + \phi + Lr \tag{41}$$

where c_p is the specific heat of air under constant pressure, ϕ is geopotential height, r is the mixing ratio of water vapor, and L is the latent heat of condensation. In this definition of total energy, the kinetic energy (being relatively small) is neglected.

In section 4, it is demonstrated that the subtropics of the Northern Hemisphere constitute a source of moisture for the model atmosphere because the rate of evaporation far exceeds the precipitation rate there. Figure 26 indicates that the northern subtropics export great amounts of moisture both northward and sourthward. A major part of this southward flux of latent energy crosses the Equator and feeds the tropical rain belt in the Southern Hemisphere of the model. The tropical rain belt in turn converts latent energy into heat energy through the condensation process and exports a great deal of heat energy back to the Northern Hemisphere. The direction of net cross-equatorial transport of total energy [(latent energy) + (heat energy)] is northward (i.e., from the summer to the winter hemisphere). However, the magnitude of this net transport is rather small because the transport of latent energy and that of heat energy have comparable magnitudes but opposite directions. In summary, the tropical rain belt in the Southern (summer) Hemisphere is chiefly maintained through the interhemispheric exchanges of heat and latent energies.

According to figure 18, which shows the latitudinal distributions of the rates of precipitation and evaporation, precipitation exceeds evaporation in middle latitudes. That is, the model atmosphere loses water vapor in middle latitudes and has to import moisture from elsewhere. Figure 26 indicates that middle latitudes receive moisture from lower latitudes and export great amounts of heat energy toward higher latitudes.

Figure 27 is presented to illustrate how this energy is transported poleward in the model atmosphere. In this figure, the northward transports of both heat and latent energy are subdivided into three parts (i.e., transports by meridional circulation, large-scale eddies, and subgrid scale mixing). According to this figure, the cross-equatorial transports of both heat and latent energy are essentially accomplished by the meridional circulation (viz, by the interhemispheric Hadley cell described in section 3). In the model subtropics, the poleward transport of latent energy by the large-scale eddies is significant. In middle latitudes, the poleward transports of both heat and latent energy are chiefly accomplished by large-scale eddies. For comparison, the northward transports in the actual atmosphere, which were obtained by Oort and Rasmusson (1970) for the Northern Hemisphere, are plotted in figure 27. The features of the observed distribution are quite similar to those of the model. Finally, it should be pointed out that the poleward transport of energy by subgrid scale mixing is practically negligible.

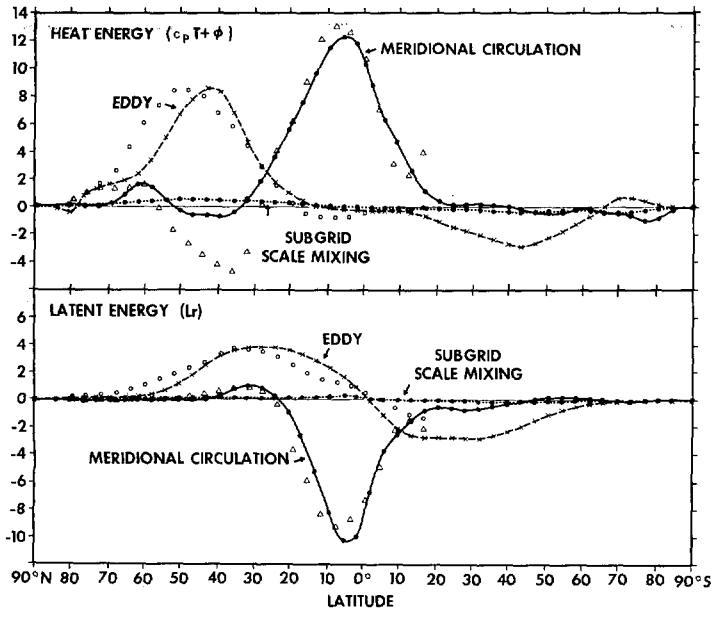

FIGURE 27.—Latitudinal distributions of the northward transport of energy ($\times 10^{19}$ cal/day) by the meridional circulation, large-scale eddies, and subgrid scale mixing. The transport values in the actual atmosphere, estimated by Oort and Rasmusson (1970) for January, are plotted by open circles (eddy) and by triangles (meridional circulation).

7. STRATOSPHERIC HEAT BALANCE

As pointed out in subsection 3A, the zonal mean temperature of the lower stratosphere of the model increases with increasing latitude in the Southern (summer) Hemisphere and is at a maximum in the Antarctic. In the Northern (winter) Hemisphere, it has a maximum value in middle latitudes. These features of the model stratosphere are in excellent qualitative agreement with those of the actual atmosphere. Therefore, it seems appropriate to discuss how the temperature distribution is maintained in the model stratosphere.

Figure 28 shows the latitude-height distribution of heat transport by the large-scale eddies and indicates that the large-scale eddies transport heat poleward in the model stratosphere in both hemispheres. The comparison between the latitudinal distribution of eddy transport and that of zonal mean temperature in the lower stratosphere of the model (see fig. 3) reveals that heat is transported against the horizontal temperature gradient in most of the lower stratosphere except in the higher latitudes of the Northern Hemisphere. Such a countergradient flux of heat in the lower stratosphere was first discovered by White (1954). This countergradient flux plays a key role in creating the temperature

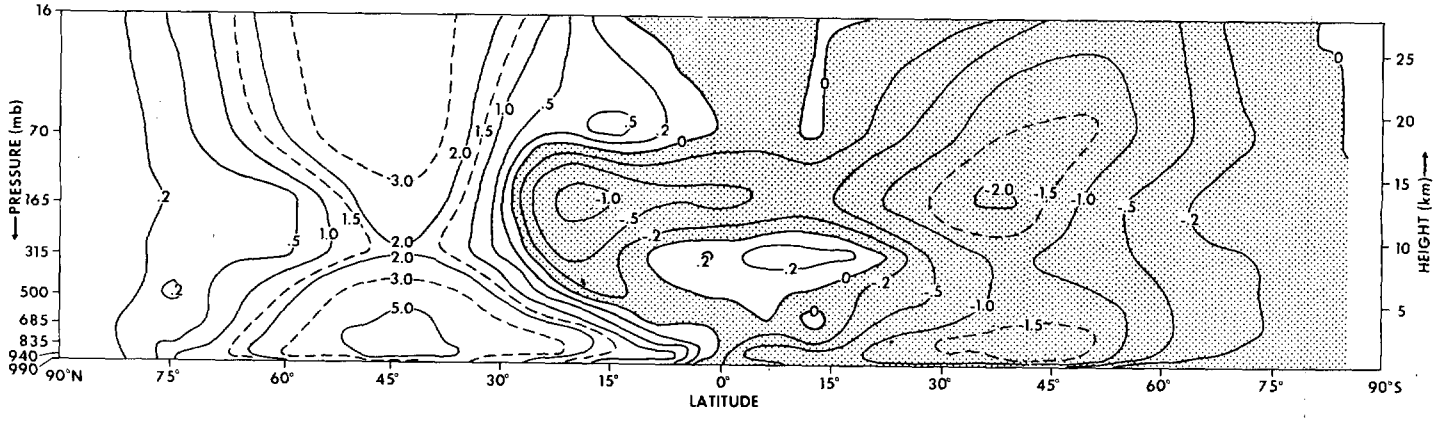

FIGURE 28.—Latitude-height distribution of the northward transport of heat by the large-scale eddies in the model atmosphere; units, 10^{17} J·mb^{-1}·day^{-1}.

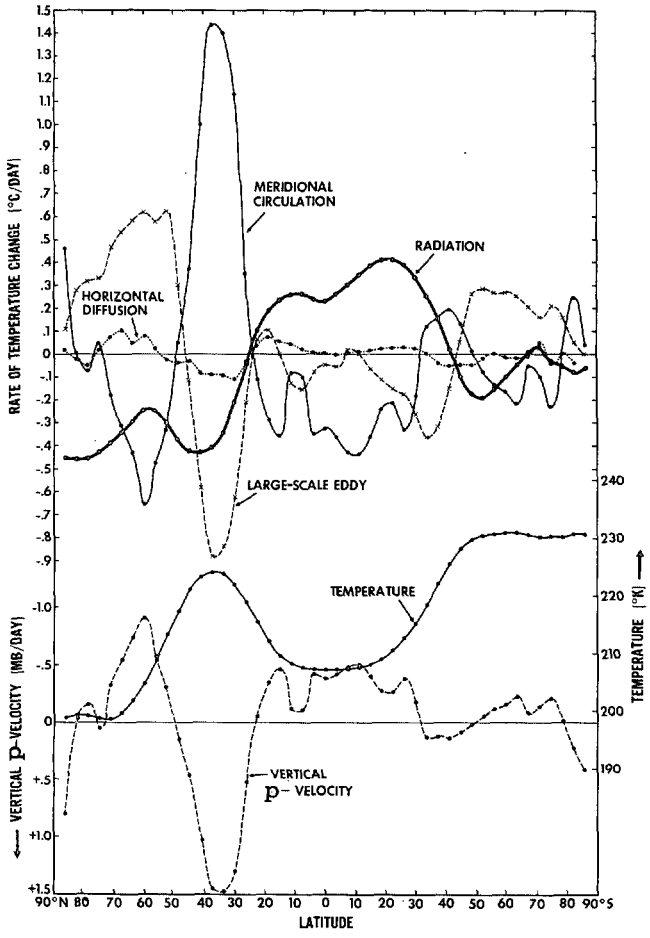

FIGURE 29.—Upper half, mean rates of temperature change by radiation, meridional circulation, large-scale eddies, and subgrid scale horizontal diffusion at the 70-mb level of the model as a function of latitude; lower half, the latitudinal distributions of zonal mean temperature and zonal mean vertical p velocity at the 70-mb level.

distribution in the model stratosphere of the summer as well as of the winter hemisphere.

For illustrating how the heat balance of the model stratosphere is maintained, the rates of temperature change by radiation, meridional circulation, large-scale eddies, and subgrid scale eddies at the 70-mb level are shown in figure 29 as a function of latitude. (Because of interpolation error in the analysis computation, the sum of all contributions in fig. 29 does not vanish exactly.) The latitudinal distributions of zonal mean temperature and zonal mean vertical p velocity at the 70-mb level are also added to the lower part of figure 29 for convenience in the discussion.[3] In the tropical stratosphere of the model, the adiabatic cooling in the upward-moving branch of the meridional circulation tends to lower the temperature and is responsible for the temperature minimum there. In middle latitudes of the Northern Hemisphere, the adiabatic heating in the downward-moving branch of the meridional circulation raises the temperature and is the chief cause of the temperature maximum at these latitudes. In both hemispheres of the model, the poleward eddy transport of heat, discussed in the preceding section, removes heat from lower latitudes, supplies heat to high latitudes, and tends to increase the temperature with increasing latitude. Although the effects of the meridional circulation and the large-scale eddies tend to compensate each other, the net contribution of these two dynamical effects is to create the existing temperature gradient in the lower stratosphere of the model. On the other hand, the radiative effect tends to destroy the temperature gradient generated by these two dynamical effects. The distributions of heat balance components in the Northern Hemisphere of the model are in excellent qualitative agreement with those obtained by Manabe and Hunt (1968) from their 18-level model.

8. CONCLUDING REMARKS

In this study, it is shown that the global model of the atmosphere that we have developed is capable of simulating, at least qualitatively, some of the major features of the hydrologic cycle and of the global climatic patterns during January. For example, the tropical rain belt, the middle-latitude rain belt, the areas of large runoff rate, and major arid regions (such as the Sahara and Australian Deserts) are successfully simulated. The horizontal distributions of the net downward radiation and the upward fluxes of sensible and latent heat at the surface of the model continents are very similar to those of the corresponding quantities obtained by Budyko (1963). The latitudinal distributions of the poleward transports of heat and latent energies in the model atmosphere also compare favorably with those in the actual atmosphere, as estimated by Oort and Rasmusson (1970). It is noteworthy that the massive, interhemispheric Hadley cell predominates in the model Tropics and transports heat energy and latent energy in opposite directions across the model Equator. This cell supplies latent energy to the tropical rain belt of the model and removes the heat energy released by condensation.

In the lower stratosphere of the model, except at high northern latitudes, the temperature increases with increasing latitude, in agreement with features of the actual stratosphere. The effect of the countergradient heat transport by the large-scale eddies, combined with the effect of the adiabatic temperature change due to the meridional circulation, is responsible for this temperature gradient in the summer as well as in the winter hemisphere of the model. The effects of radiative transfer tend to destroy this temperature gradient.

There are various indications that the global model used for this study has a systematic bias toward developing excessively high pressure in polar regions. Furthermore, the model tends to overpredict the relative humidity near the earth's surface. The development of a model free of such biases seems to be essential for the satisfactory simulation of climate.

[3] As pointed out in section 3, the latitudinal distributions of various quantities in the model atmosphere are shifted systematically toward the Equator from their observed counterparts. Therefore, one should keep this bias in mind when examining these results.

It is suggested that the perpetual January insolation, assumed for this study, is partly responsible for the unrealistically low temperatures in the Arctic. A natural extension of this study would be a simulation of the seasonal variation of climate by a model incorporating the effects of the seasonal variation of insolation.

One of the probable future applications of mathematical models of climate is in the evaluation of the possibility of climatic change caused by human activity. For example, it is important to know how the increase in carbon dioxide content in the atmosphere, resulting from fossil fuel combustion, affects the climate. Since climatic change often causes changes in oceanic temperatures, which in turn affect the climate, one cannot predict the global change of climate by using a model with a given distribution of sea-surface temperatures. It is, therefore, desirable to combine a mathematical model of the atmosphere with an ocean model, such as the one developed by Bryan and Cox (1967), to create a joint ocean-atmosphere model. In such a model, the sea-surface temperatures are determined as a result of coupling between the model ocean and the model atmosphere. Recently, Manabe and Bryan (1969) constructed such a joint model with highly idealized topography. The construction of a joint ocean-atmosphere model with realistic topography is a next major goal of our research.

APPENDIX A—COMPUTATIONAL TECHNIQUES

A. TIME INTEGRATION

The time step for the integration of the low-resolution grid (N24) model is 400 s, and that for the high-resolution grid (N48) is 300 s. Experimentation shows that the high-resolution model remains stable with a 300-s time step as well as with one of 200 s or half the N24 value. Therefore, the longer time step is used to save computer time.

For preventing the growth of a computational mode, the wind, temperature, humidity, and pressure fields at three consecutive time steps are averaged once every 53 time steps by the weights 0.25, 0.5, and 0.25. After such a smoothing time step, one noncentral time extrapolation is performed before the normal leapfrog time integration is restarted.

As an additional precaution, the high-resolution (N48) model time integration is performed by a so-called "Euler backward" scheme proposed by Matsuno (1966) for 12 time steps out of every 288 or every simulation day [see Manabe et al. (1970*a*) for further details on this system]. This procedure is done to prevent the development of high-frequency gravity waves that tend to appear in high-resolution model experiments. During this procedure, the time-step length is left unchanged.

B. REVISED PRESSURE GRADIENT FORMULATION

Equations (1) and (2) contain two terms for evaluating the pressure gradient (i.e., a derivative of geopotential on the σ surfaces and a surface pressure gradient term, which corrects the σ surface geopotential gradient to one on constant pressure surfaces). The pressure gradient correction term is adequate for models without mountains; but in models with realistic topography, the two-term pressure gradient evaluation permits large truncation error and is responsible for a checkerboard pattern in the surface-pressure field. This truncation error is markedly reduced by use of a single pressure-gradient term, as suggested by Sangster and Smagorinsky (Smagorinsky et al. 1967). In the east-west direction, this single term is

$$-p_*\left(\frac{\partial\phi}{a\cos\theta\partial\lambda}\right)_p.$$

This term is evaluated on a constant pressure surface defined by a given σ level at the central grid point. This pressure is obtained by the product of surface pressure at this point and the given σ value. Geopotentials at all surrounding grid points involved in the gradient computation are computed by a build-up from the surface to the specified constant pressure surfaces. When constant pressure surfaces fall below the earth's surface at a grid point, geopotentials are estimated under the assumption of a locally-representative effective temperature of air between the $\sigma=1$ level and the specified pressure level. A similar form of this single-gradient term can be derived in the north-south direction.

C. REVISED VERTICAL PRESSURE-VELOCITY EQUATION

The original version of the vertical p-velocity eq (8) generates large irregularities in the field of vertical motion and thereby adversely affects the temperature field in the stratosphere where the static stability is very high. Such irregularities propagate downward through the pressure interaction term and generate irregularities in the troposphere. The field of surface pressure p_* has small-scale patterns because of the uneven topography. Therefore, the advection term of surface pressure on the right-hand side of eq (8) generates intense small-scale vertical motions. Miyakoda (1967) pointed out that this difficulty can be avoided by use of an alternate form of the equation of ω, originally suggested by Smagorinsky (1962). This form of the equation does not involve the horizontal advection of surface pressure. The new vertical p-velocity formulation derived below was incorporated into the model as soon as this model deficiency was discovered. It was put into the model between the averaging period for the hydrologic means and the period of averaging for the zonal wind fields, and it was used for the entire high-resolution time integration.

The vertical p-velocity equation is derived from the vertical σ-velocity $\dot{\sigma}$ and the definitions of ω and σ as follows:

$$p=\sigma p_* \tag{42}$$

and

$$\omega=\frac{dp}{dt}. \tag{43}$$

Therefore,

$$\omega=p_*\frac{d\sigma}{dt}+\sigma\frac{dp_*}{dt}$$
$$=p_*\dot{\sigma}+\sigma\left[\frac{\partial p_*}{\partial t}+\mathbf{V}\cdot\nabla_H p_*\right]. \quad (44)$$

Equation (44) is equivalent to eq (8). In the σ coordinate system, the continuity equation may be written as

$$\frac{\partial p_*}{\partial t}=-p_*\frac{\partial\dot{\sigma}}{\partial\sigma}-\nabla_H\cdot(p_*\mathbf{V}). \quad (45)$$

Substituting the surface pressure tendency of eq (45) into eq (44), we obtain

$$\omega=p_*\sigma\left[\frac{\dot{\sigma}}{\sigma}-\frac{\partial\dot{\sigma}}{\partial\sigma}-\nabla_H\cdot\mathbf{V}\right] \quad (46)$$

where

$$\nabla_H\cdot\mathbf{V}=\frac{\partial u}{a\cos\theta\partial\lambda}+\frac{\partial(v\cos\theta)}{a\cos\theta\partial\theta}. \quad (47)$$

D. SHORTCOMINGS OF THE KURIHARA GRID

The Kurihara computational grid used for the models described in this paper was developed at GFDL to allow the hydrodynamical equations to be integrated over the entire globe without horizontal boundaries. It provides reasonably uniform resolution in all directions and over the entire domain. However, the finite-difference solutions to the equations solved on this grid suffer from some deficiencies of the grid, which we shall point out in this subsection.

Recently, Rao and Umscheid (1969) carried out a series of test computations on a barotropic model solved on the Kurihara grid system. Their results reveal that the model tends to develop an area of high pressure around the Pole, unless they chose a very high computational resolution. A similar bias is evident when we compare results from a baroclinic model, using the Kurihara grid (Kurihara and Holloway 1967), with those from a similar model, having a rectangular array of comparable grid size (Smagorinsky et al. 1965).

As known, finite-difference approximations computed on the Kurihara grid are accurate only to the first order, whereas those computed on regular grids have second-order accuracy. This results in lowering the effective resolution of the Kurihara grid somewhat below that of a regular grid having the same mean grid spacing. It is very probable that the excessive polar High described in subsection 3C is partly due to the poor accuracy of the computation on an irregular grid. This speculation is substantiated by figure 7, which indicates a significant lowering of polar pressures resulting from the increase in computational resolution. The magnitude of the pressure decrease, however, is far from sufficient. It is likely that the truncation error of the finite-difference computation is particularly large in the polar region where the curvature of the curvilinear coordinate (i.e., latitude circles) is at a maximum.

Finally, Shuman (1970) showed an example of large truncation errors arising from a finite-difference computation in a polar region. It is related to the manner in which wind vectors are averaged in the application of the box method to this grid. The vector components of the wind, on the interfaces between pairs of boxes, are computed as the arithmetic means of the components at the centers of the boxes that meet at these interfaces. This computation is done without regard to the slight differences in the directions of the unit vectors, located at the adjacent grid points involved. This approximation used in averaging vector components is most inaccurate near the Poles where the directions of the unit vectors change most rapidly from one box to the next. As pointed out by Dey (1969), this approximation creates fictitious horizontal convergence upwind of the Pole and false divergence downwind of the Pole when air flows across the Pole. The fact that these patterns of convergence and divergence are not centered on the Pole suggests that there is no connection between this finite-difference error and the high-pressure phenomenon at the Poles.

However, despite these finite-difference inaccuracies inherent in the Kurihara grid, we were able to time integrate our model over the entire globe successfully for several hundred simulation days. Apparently, the errors near the Poles are not serious enough to degrade the results of the atmospheric simulation appreciably in middle and low latitudes, especially at high resolution.

One method for reducing the various finite-difference errors described above is to increase the resolution of the grid on which the computations are performed. Partly for this reason, the resolution of the grid was doubled and the model experiment described in this paper was repeated. Some of the results of this high-resolution-model experiment are presented in appendix B.

APPENDIX B—SOME RESULTS FROM THE HIGH-RESOLUTION MODEL

Manabe et al. (1970*a*) demonstrated that the results from a hemispheric general circulation model are markedly improved by reducing the mean grid spacing from 500 to 250 km. Therefore, we decided to integrate the model equations on a finer horizontal grid network for as many simulation days as practical, considering the enormous amount of computer time required for these high-resolution calculations. The Univac 1108 electronic computer[4] requires about 27 hr of real time to integrate a 24-hr atmospheric simulation at high resolution. There are 9,216 grid points in the high-resolution model with 48 grid points between the Poles and the Equator and 192 around the Equator. The grid distances vary from 208

[4] Mention of a commercial product does not constitute an endorsement.

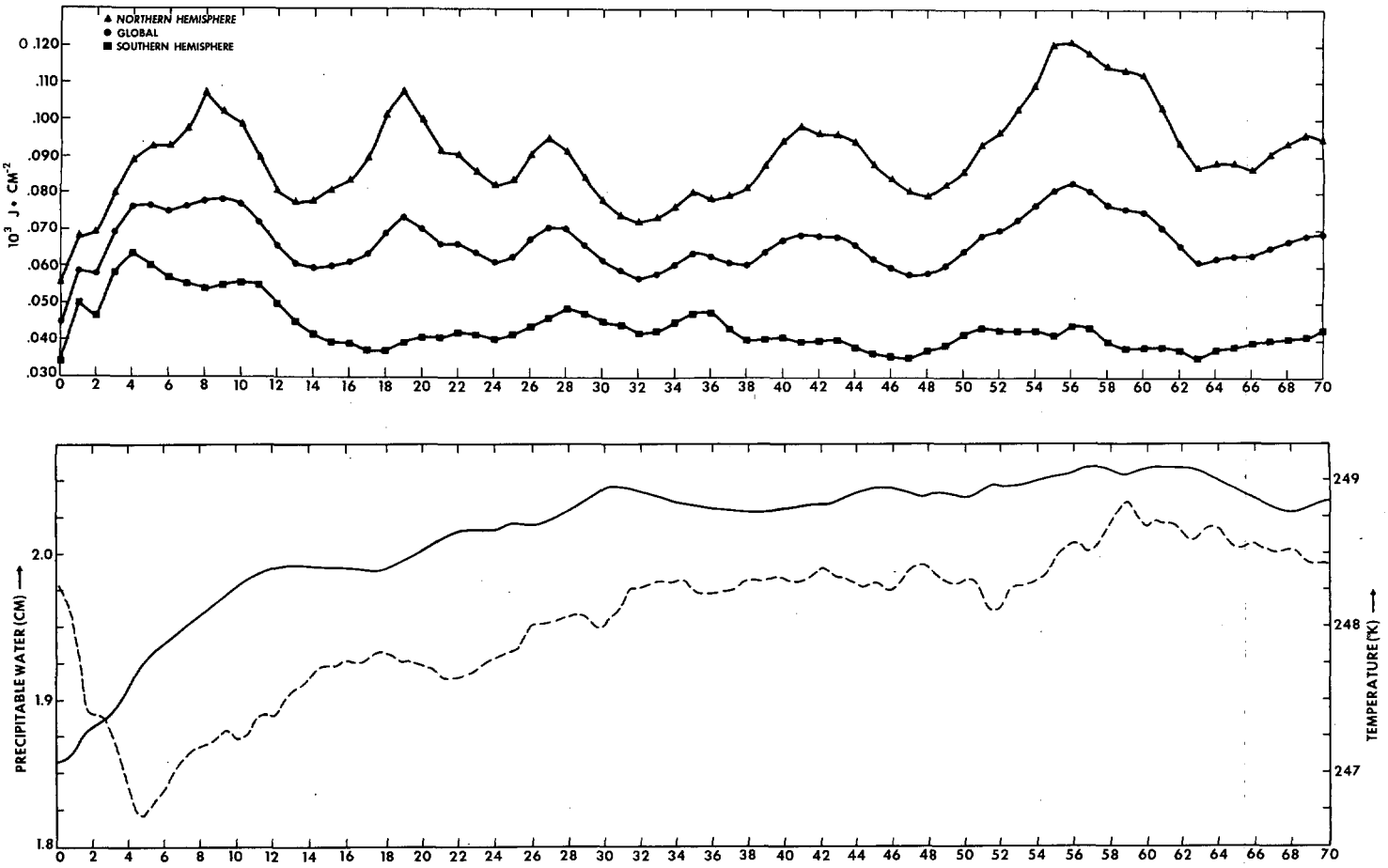

FIGURE 30.—Time variations of (upper graph) the global and hemispheric means of the eddy kinetic energy in the N48 model experiment and of (lower graph) the global means of temperature (solid line) and precipitable water (dashed line). The time in days is along the abscissa.

to 325 km. Hereafter, this grid will be called N48, and the low-resolution grid, N24. Results from the N48 model experiment are compared with those of the N24 experiment in this appendix whenever the increase in resolution made a significant change in the model simulations. The derivation of the high-resolution smoothed topography is described in appendix C.

The data fields from the N24 model at simulation day 302 are linearly interpolated to the N48 grid as input for the high-resolution model experiment. The N48 model is time integrated for 70 days beyond this initial time. Figure 30 shows the time variations of the hemispheric and global mean values of the eddy kinetic energy and the time series of the global means of the temperature and precipitable water during this 70-day period. Obviously, it would have been desirable to extend the integration for a longer period of time to approach more closely a state of quasi-equilibrium. However, the experiment is terminated on the 70th day because of the enormous amount of machine time required for integrating each simulation day of this high-resolution model. Various quantities, shown in this appendix, represent the average state of the 36 days inclusively from the 35th to the 70th model day. Because of the great variability of precipitation and other hydrologic quantities, it would have been desirable to time average over a longer period. Unfortunately, the shortage of computer time limited the averaging period so that the lack of a stable mean offsets some of the gain in accuracy obtained by the high-resolution computation.

The zonal mean sea level pressure, averaged over the 36-day period at the end of the N48 model experiment, appears in figure 7 presented in section 3. The latitudes and intensities of the pressure maxima in the northern and southern subtropics are significantly improved by the increase in the horizontal resolution of the finite differencing. The latitudes of the low-pressure minima in middle latitudes are closer to the Poles and to the observed locations in the N48 results than in the pressure distribution simulated by the N24 model experiment. In both hemispheres, the mean observed minima are at about 68° latitude. In the Northern Hemisphere, the N48 model simulates a low-pressure trough at about 58°N, whereas the N24 trough is as far south as 48°N. In the Southern Hemisphere, the discrepancy is even greater; but again, the low-pressure trough is situated closer to the observed location in the high-resolution-model experi-

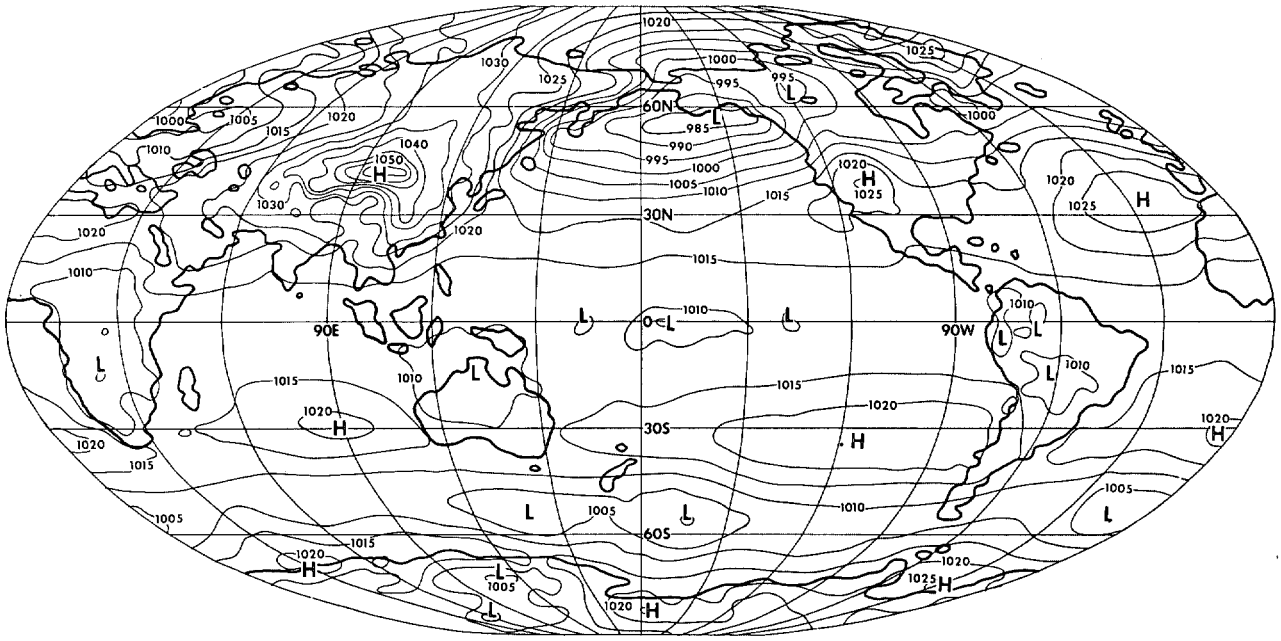

FIGURE 31.—Global distribution of mean sea level pressure during the 36-day averaging period for the N48 resolution model experiment; units, mb.

ment. The computed polar pressures are far above normal in the N48 model experiment; but in the Northern Hemisphere, they are, nevertheless, considerably closer to observed values than those of the N24 resolution results. In summary, the increase in the horizontal computational resolution produces a poleward shift of the sea-level pressure patterns coupled with an increase in the amplitude of the meridional variation of pressure in middle and low latitudes.

Figure 31 presents a map of the global distribution of the mean sea level pressure during the 36-day averaging period for the N48 resolution model experiment. This figure should be compared with the mean observed sea-level pressure distribution and that obtained by the N24 model, both of which are shown in figure 8.

In the Northern Hemisphere, the increase in the horizontal resolution on the whole improves the simulation of the centers of high and low pressure over what is obtained at lower resolution. For example, the pressures at the Pole are reduced to values much closer to climatic means. The Siberian High is much better developed in the N48 results and is now practically detached from the polar High. The reduction in the excessively high, north polar pressure decreases the fictitiously strong pressure gradient to the north of the Aleutian Low seen on the N24 map. As a result, the Aleutian Low itself is moved northward for a closer agreement with the mean observed sea-level pressure in this area. Unfortunately, the Icelandic Low is not improved in the high-resolution integration.

The subtropical high-pressure belt in figure 31 is much more clearly defined in both the Northernd an Southern Hemispheres than at the N24 resolution. In the Southern Hemisphere, the Lows in the middle-latitude storm belt are located farther south, in better agreement with observations. Furthermore, the pressure difference between the subtropical Highs and the middle-latitude Lows is greater. This improvement in turn improves the simulation of the surface westerlies in high southern latitudes.

The mean precipitation rate computed by the N48 resolution model is shown in figure 32. This figure should be compared with the observed precipitation rate presented in the lower half of figure 12. On the whole, the high-resolution precipitation simulations are considerably better than the N24 computations although the N48 results tend to be less smooth, in part, because the averaging period is half as long as that for the low-resolution mean.

In the Northern Hemisphere, the middle-latitude precipitation belt is simulated better at high resolution than at low. The improvement probably can be attributed as much to the more accurate topography as to the generally better simulation of the dynamics of the atmosphere provided by the finer computational grid. The centers of high precipitation rate over the oceans and extending into the continents are interspersed with drier areas centered on the continents. In agreement with the climatic data, these areas of low precipitation rate, computed by the N48 model on the continents, extend from the subtropical dry belt to the polar regions of low precipitation. The dry areas in Asia and in North America

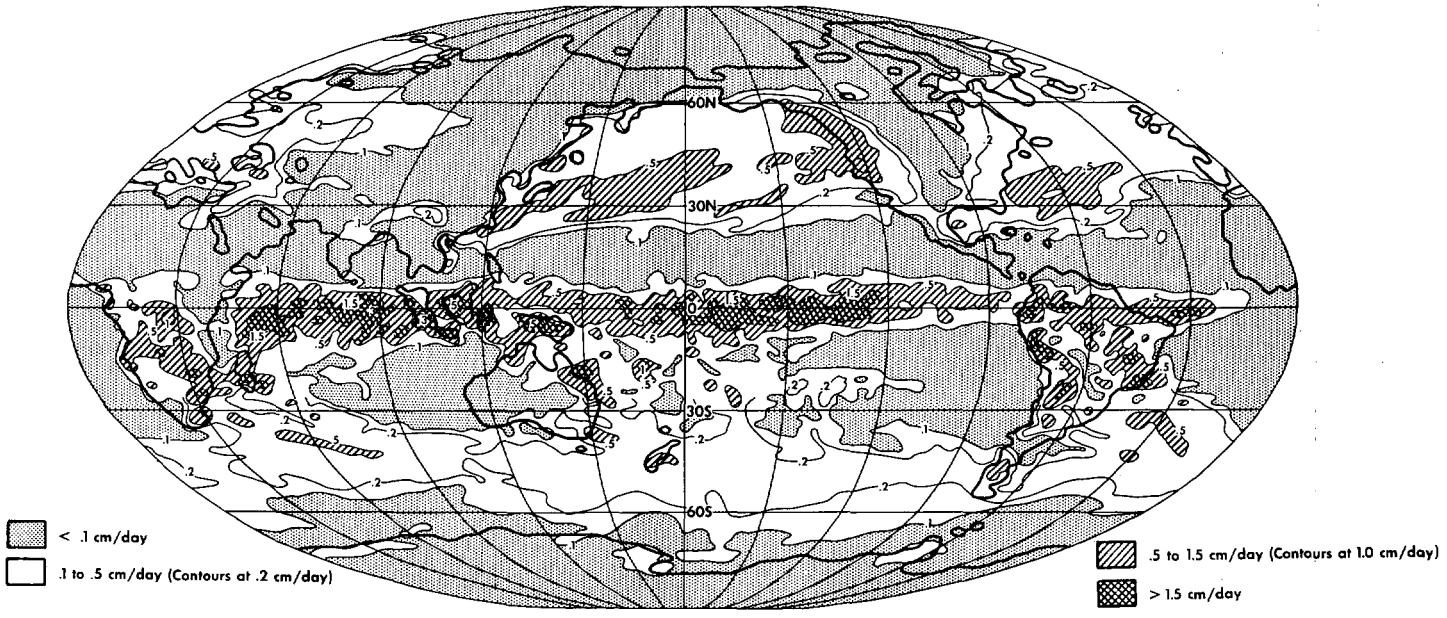

FIGURE 32.—Mean global precipitation rates computed by the high resolution (N48) model experiment.

are wider in the N48 model results, in better agreement with observation.

In the Tropics, the rain belt obtained by the high-resolution model is narrower than in the N24 experiment. Partly because of the relatively short averaging period, some roughness appears in the rainfall patterns. The high-resolution rainfall distribution lacks the spur of high rainfall, which appears in the observed map and even in the N24 results, extending from the central equatorial Pacific toward southern South America.

In the Southern Hemisphere, the regions of low precipitation rate over the subtropical oceans do not extend as far inland on the West Coasts of southwestern Africa and southern South America as in the N24 experiment, in good agreement with observation. This improvement in simulation is, no doubt, attributable to the higher mountains in the high-resolution model. These taller mountains are more effective in blocking dry air from flowing out of the dry anticyclones, situated off the west coasts of Africa and South America. As pointed out earlier, the N48 topography is less smooth and higher, especially in regions of narrow mountain ranges such as the Andes, than the topography used in the N24 model experiment (see appendix C).

In both hemispheres, the computed middle-latitude belts of maximum precipitation rate are slightly more intense and are located at somewhat higher latitudes in the N48 results than in those of the low-resolution experiment. These positions correspond more closely to their observed latitudes and strengths. This improvement is correlated with the more realistic pressure distribution at these latitudes.

421-361 O—71——3

APPENDIX C—DERIVATION OF THE SMOOTHED TOPOGRAPHY

The topography used in the N24 model experiment is shown in figure 33. The basic data for the mountain heights came from a computer tape produced by the Scripps Institution of Oceanography (Smith et al. 1966). For the N24 grid, these Scripps data are interpolated to the Kurihara grid and smoothed by the repeated application of the following space smoothing function:

$$\bar{z}=0.5\, z_0+\sum_{i=1}^{N} (w_i z_i) \tag{48}$$

where z_0 is the raw unsmoothed height at the central grid point, z_i is the height at the surrounding grid point i, w_i is a weighting factor proportional to the length of the interface between the box i and the central box (normalized so as to make the sum of the weights equal to one-half), and $\bar{z}$ is the resulting smoothed height. The summation is over all N surrounding contiguous boxes in the grid.

Three applications of this smoothing function give the desired degree of smoothing. It is, of course, necessary to smooth the topography until the scale of variations in land height matches the resolution of the grid. The Scripps data contain ocean-bottom topography as negative values in addition to positive land-height values. All data are used; and when a negative smoothed height results at a grid point which had been above sea level in the input data, the original shoreline is restored (i.e., the height is redefined as a positive 1 m).

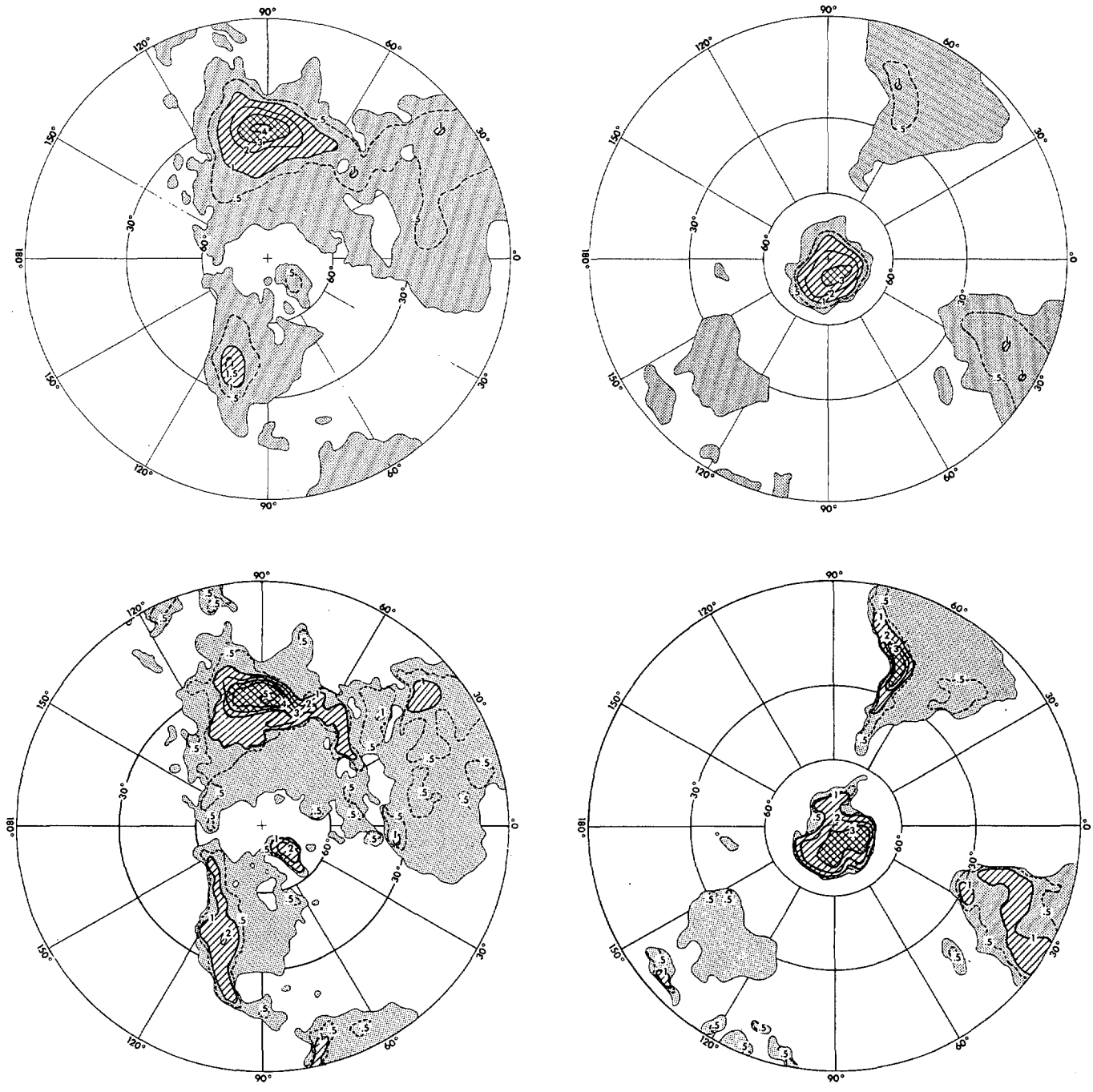

FIGURE 33.—Polar stereographic maps of the continental boundaries and mountain heights in the Northern (left) and Southern (right) Hemispheres of the N24 (upper) and N48 (lower) resolution grids. Areas with elevations > 1 km are shaded with slashed lines and those >3 km with checkered lines.

The topography for the high resolution (N48) model is derived slightly differently from that for the N24 grid. The interpolation and smoothing are performed in one operation by weighting data on the Scripps grid network (in most areas spaced every degree of latitude and longitude) by a function of the great circle distance from the location of the Scripps data to the particular Kurihara grid point for which the smoothed terrain height is being computed. The weighting function is a two-dimensional normal curve truncated at a radius of 200 km, at which distance the weight is 13.5 percent of that at the origin. The computation of a typical smoothed height involves an average of about 12 Scripps data points. The restoration of the continental shorelines after smoothing is done by a method similar to that used for the N24 grid (i.e., the land or sea status of a grid point is determined by the

land-sea status of the nearest Scripps data point). Mathematical eroding of the coasts is reduced by halving the ocean depths before smoothing the combined land-ocean-bottom topography. The resolutions of the N24 and N48 grid networks are illustrated by the degree of smoothing and simplication of the continental outlines of the N24 maps in sections 3 and 4 and of the N48 maps in appendix B. Maps of the N48 topography are shown in the lower half of figure 33. Notice that the Rocky Mountains in North America and the Andes in South America are somewhat taller and more narrow on the high-resolution grid.

ACKNOWLEDGMENTS

The authors gratefully acknowledge the many useful suggestions provided by Dr. Y. Kurihara for improving the model and enabling us to carry out a successful integration. We wish to express our appreciation to Dr. J. Smagorinsky for his encouragement and valuable support and to Dr. K. Miyakoda for his very valuable advice for solving some of our computational difficulties. We are indebted to Mr. R. Wetherald for programming the computations of the hydrologic scheme in the model. We also wish to thank Mrs. W. Carlton who wrote a substantial part of the computer programs for the model and the analysis computation. Finally, we are greatly indebted to all of the members of the GFDL staff who assisted with the preparation of the manuscript and figures and in particular to Mr. L. Dimmick.

REFERENCES

Bryan, Kirk, and Cox, Michael D., "A Numerical Investigation of the Oceanic General Circulation," *Tellus*, Vol. 19, No. 1, Stockholm, Sweden, Feb. **1967**, pp. 54–80.

Budyko, M. I., *Teplovoĭ balans Zemnoĭ Poverkhnosti* (Heat Balance of the Earth's Surface), Gidrometeorologicheskoe Izdatel'stvo, Leningrad, U.S.S.R., **1956**, 254 pp.

Budyko, M. I. (Editor), *Atlas Teplovogo Balansa Zemnogo Shara* (Guide to the Atlas of the Heat Balance of the Earth), Gidrometeoizdat, Moscow, U.S.S.R., **1963**, 69 pp.

Crutcher, Harold L., and Meserve, J. M., "Selected Level Heights, Temperatures and Dew Points for the Northern Hemisphere," *NAVAIR* 50-1C-52, U.S. Naval Weather Service, Washington, D.C., Jan. **1970**, 8 pp. and numerous charts.

Dey, Clifford H., "A Note on Global Forecasting With the Kurihara Grid," *Monthly Weather Review*, Vol. 97, No. 8, Aug. **1969**, pp. 597–601.

Gerdel, Robert Wallace, "The Transmission of Water Through Snow," *Transactions of the American Geophysical Union*, Vol. 35, No. 3, June **1954**, pp. 475–485.

Hering, Wayne S., and Borden, Thomas R., Jr., "Mean Distributions of Ozone Density Over North America, 1963–1964," *Environmental Research Papers*, No. 162, U.S. Air Force Cambridge Research Laboratories, Hanscom Field, Mass., Dec. **1965**, 19 pp.

Kasahara, Akira, and Washington, Warren M., "Thermal and Dynamical Effects of Orography on the General Circulation of the Atmosphere," *Proceedings of the WMO/IUGG Symposium on Numerical Weather Prediction, Tokyo, Japan, November 26–December 4, 1968*, Japan Meteorological Agency, Tokyo, Mar. **1969**, pp. IV-47—IV-56.

Kung, Ernest C., Bryson, Reid A., and Lenschow, Donald H., "Study of a Continental Surface Albedo on the Basis of Flight Measurements and Structure of the Earth's Surface Cover Over North America," *Monthly Weather Review*, Vol. 92, No. 12, Dec. **1964**, pp. 543–564.

Kurihara, Yoshio, "Numerical Integration of the Primitive Equations on a Spherical Grid," *Monthly Weather Review*, Vol. 93, No. 7, July **1965**, pp. 399–415.

Kurihara, Yoshio, and Holloway, J. Leith, Jr., "Numerical Integration of a Nine-Level Global Primitive Equations Model Formulated by the Box Method," *Monthly Weather Review*, Vol. 95, No. 8, Aug. **1967**, pp. 509–530.

Leith, Cecil E., "Numerical Simulation of the Earth's Atmosphere," *Methods in Computational Physics, Volume 4. Applications in Hydrodynamics*, Academic Press, New York, N.Y., **1965**, 385 pp. (see pp. 1–28).

London, Julius, "A Study of the Atmospheric Heat Balance," *Final Report*, Contract No. AF19(122)-165, Department of Meteorology and Oceanography, New York University, N.Y., July **1957**, 99 pp.

London, Julius, "Mesospheric Dynamics: Part III. The Distribution of Total Ozone in the Northern Hemisphere," *Final Report*, Contract No. AF19(604)-5492, Department of Meteorology and Oceanography, New York University, N.Y., May **1962**, pp. 68–108.

Manabe, Syukuro, "Climate and the Ocean Circulation: I. The Atmospheric Circulation and the Hydrology of the Earth's Surface," *Monthly Weather Review*, Vol. 97, No. 11, Nov. **1969**, pp. 739–774.

Manabe, Syukuro, and Bryan, Kirk, "Climate Calculations With a Combined Ocean-Atmosphere Model," *Journal of the Atmospheric Sciences*, Vol. 26, No. 4, July **1969**, pp. 786–789.

Manabe, Syukuro, and Holloway, J. Leith, Jr., "Climate Modification and a Mathematical Model of Atmospheric Circulation," *A Century of Weather Progress*, American Meteorological Society, Boston, Mass., **1970***a*, pp. 157–164.

Manabe, Syukuro, and Holloway, J. Leith, Jr., "Simulation of the Hydrologic Cycle of the Global Atmospheric Circulation by a Mathematical Model," *Proceedings of the Reading, England, Symposium, July 15–23, 1970, IASH–UNESCO Publication* No. 92, International Association of Scientific Hydrology, Gentbrugge, Belgium, July **1970***b*, pp. 387–400.

Manabe, Syukuro, and Holloway, J. Leith, Jr., "Simulation of Climate by a Global General Circulation Model: II. Effect of Mountains," U.S. Department of Commerce, Geophysical Fluid Dynamics Laboratory, Princeton, N.J., **1971** (unpublished study).

Manabe, Syukuro, Holloway, J. Leith, Jr., and Stone, Hugh M., "Tropical Circulation in a Time Integration of a Global Model of the Atmosphere," *Journal of the Atmospheric Sciences*, Vol. 27, No. 4, July **1970***b*, pp. 580–613.

Manabe, Syukuro, and Hunt, Barrie G., "Experiments With a Stratospheric General Circulation Model: I. Radiative and Dynamic Aspects," *Monthly Weather Review*, Vol. 96, No. 8, Aug. **1968**, pp. 477–502.

Manabe, Syukuro, and Smagorinsky, Joseph, "Simulated Climatology of a General Circulation Model With a Hydrologic Cycle: II. Analysis of the Tropical Atmosphere," *Monthly Weather Review*, Vol. 95, No. 4, Apr. **1967**, pp. 155–169.

Manabe, Syukuro, Smagorinsky, Joseph, Holloway, J. Leith, Jr., and Stone, Hugh M., "Simulated Climatology of a General Circulation Model With a Hydrologic Cycle: III. Effects of Increased Horizontal Computational Resolution," *Monthly Weather Review*, Vol. 98, No. 3, Mar. **1970***a*, pp. 175–212.

Manabe, Syukuro, Smagorinsky, Joseph, and Strickler, Robert F., "Simulated Climatology of a General Circulation Model With a Hydrologic Cycle," *Monthly Weather Review*, Vol. 93, No. 12, Dec. **1965**, pp. 769–798.

Manabe, Syukuro, and Strickler, Robert F., "Thermal Equilibrium of the Atmosphere With a Convective Adjustment," *Journal of the Atmospheric Sciences*, Vol. 21, No. 4, July **1964**, pp. 361–385.

Manabe, Syukuro, and Wetherald, Richard T., "Thermal Equilibrium of the Atmosphere With a Given Distribution of Relative Humidity," *Journal of the Atmospheric Sciences*, Vol. 24, No. 3, May **1967**, pp. 241–259.

Mastenbrook, H. J., "Frost-Point Hygrometer Measurements in the Stratosphere and the Problem of Moisture Contamination," *Humidity and Moisture—Measurement and Control in Science and Industry, Volume 2: Applications*, Reinhold Publishing Corp., New York, N.Y., **1965**, pp. 480–485.

Matsuno, Taroh, "Numerical Integrations of Primitive Equations by Use of a Simulated Backward Difference Method," *Journal of the Meteorological Society of Japan*, Vol. 44, No. 1, Tokyo, Feb. **1966**, pp. 76–84.

Mintz, Yale, "Very Long-Term Global Integration of the Primitive Equations of Atmospheric Motion: An Experiment in Climate Simulation," *Meteorological Monographs*, Vol. 8, No. 30, American Meteorological Society, Boston, Mass., Feb. **1968**, pp. 20–36.

Miyakoda, Kikuro, "Some Characteristic Features of Winter Circulation in the Troposphere and the Lower Stratosphere," *Technical Report* No. 14, Contract No. NSF–GP–471, Department of the Geophysical Sciences, University of Chicago, Ill., Dec. **1963**, 93 pp.

Miyakoda, Kikuro, Geophysical Fluid Dynamics Laboratory, NOAA, Princeton, N.J., **1967** (personal communication).

Möller, Fritz, "Vierteljahrskarten des Niederschlags für die Ganze Erde" (Quarterly Charts of Rainfall for the Whole Earth), *Petermanns Geographische Mitteilungen*, Vol. 95, No. 1, Justus Perthes, Gotha, East Germany, **1951**, pp. 1–7.

Murgatroyd, R. J., "Some Recent Measurements by Aircraft of Humidity up to 50,000 Feet in the Tropics and Their Relationship to Meridional Circulation," *Proceedings of the Symposium on Atmospheric Ozone, Oxford, England, July 20–25, 1959*, IGGU, Paris, France, **1960**, 30 pp.

Newell, R. E., Vincent, D. G., Dopplick, T. G., Ferruzza, D., and Kidson, J. W., "The Energy Balance of the Global Atmosphere," *The Global Circulation of the Atmosphere*, American Meteorological Society, Boston, Mass., **1969**, pp. 42–90.

Oort, Abraham H., and Rasmusson, Eugene M., "On the Annual Variation of the Monthly Mean Meridional Circulation," *Monthly Weather Review*, Vol. 98, No. 6, June **1970**, pp. 423–442.

Penn, Samuel, "The Prediction of Snow vs. Rain," *Forecasting Guide* No. 2, U.S. Weather Bureau, Washington, D.C., Nov. **1957**, 29 pp.

Phillips, Norman A., "The General Circulation of the Atmosphere: A Numerical Experiment," *Quarterly Journal of the Royal Meteorological Society*, Vol. 82, No. 352, London, England, Apr. **1956**, pp. 123–164.

Phillips, Norman A., "A Coordinate System Having Some Special Advantages for Numerical Forecasting," *Journal of Meteorology* Vol. 14, No. 2, Apr. **1957**, pp. 184–185.

Posey, Julian W., and Clapp, Philip F., "Global Distribution of Normal Surface Albedo," *Geofisica International*, Vol. 4, No. 1, Mexico City, D. F., Mexico, **1964**, pp. 33–48.

Rao, M. Sanker, and Umscheid, Ludwig, Jr., "Tests of the Effect of Grid Resolution in a Global Prediction Model," *Monthly Weather Review*, Vol. 97, No. 9, Sept. **1969**, pp. 659–664.

Richtmyer, Robert D., "Difference Methods for Initial-Value Problems," *Interscience Tracts in Pure and Applied Mathematics* No. 4, Interscience Publishers, Inc., New York, N.Y., **1957**, 238 pp. (see pp. 101–104).

Shuman, Frederick G., "On Certain Truncation Errors Associated With Spherical Coordinates," *Journal of Applied Meteorology*, Vol. 9, No. 4, Aug. **1970**, pp. 564–570.

Smagorinsky, Joseph, Geophysical Fluid Dynamics Laboratory, NOAA, Princeton, N.J., **1962** (personal communication).

Smagorinsky, Joseph, "General Circulation Experiments With the Primitive Equations: I. The Basic Experiment," *Monthly Weather Review*, Vol. 91, No. 3, Mar. **1963**, pp. 99–164.

Smagorinsky, Joseph, Manabe, Syukuro, and Holloway, J. Leith, Jr., "Numerical Results From a Nine-Level General Circulation Model of the Atmosphere," *Monthly Weather Review*, Vol. 93, No. 12, Dec. **1965**, pp. 727–768.

Smagorinsky, Joseph, Strickler, Robert F., Sangster, W. E., Manabe, Syukuro, Holloway, J. Leith, Jr., and Hembree, G. D., "Prediction Experiments With a General Circulation Model," *Proceedings of the International Symposium on Dynamics of Large-Scale Processes in the Atmosphere, Moscow, U.S.S.R., June 23–30, 1965*, Izdatel'stvo "Nauka," Moscow, **1967**, pp. 70–134.

Smith, S. M., Menard, H. W., and Sharman, G. F., "World-Wide Ocean Depths and Continental Elevations Averaged for Areas Approximating One Degree Squares of Latitude and Longitude," *S.I.O. Reference Report* 65–8, Scripps Institution of Oceanography, La Jolla, Calif., Mar. **1966**, 14 pp.

Stone, Hugh M., and Manabe, Syukuro, "Comparison Among Various Numerical Models Designed for Computing Infrared Cooling," *Monthly Weather Review*, Vol. 96, No. 10, Oct. **1968**, pp. 735–741.

Száva-Kováts, József, "Verteilung der Luftfeuchtigkeit auf die Erde" (Distribution of the Humidity of the Air Over the Earth), *Annalen der Hydrographie und Maritimen Meteorologie*, Vol. 66, No. 8, Ernest Siegfried Mittler & Sohn, Berlin, Germany, **1938**, pp. 373–378.

Taljaard, J. J., van Loon, H., Crutcher, H. L., and Jenne, R. L., "Climate of the Upper Air: Part 1. Southern Hemisphere, Volume 1. Temperatures, Dew Points, and Heights at Selected Pressure Levels," *NAVAIR* 50–1C–55, U.S. Naval Weather Service, Washington, D.C., Sept. **1969**, 6 pp. plus 134 figures.

Telegadas, Kosta, and London, Julius, "A Physical Model of the Northern Hemisphere Troposphere for Winter and Summer," *Scientific Report* No. 1, Contract No. AF19(122)–165, College of Engineering, New York University, N.Y., Feb. **1954**, 55 pp.

Teweles, Sidney, "The Energy Balance of the Stratosphere," *WMO Technical Note* No. 70, World Meteorological Organization, Geneva, Switzerland, **1965**, pp. 107–122.

U.S. Hydrographic Office, "World Atlas of Sea Surface Temperatures, Second Edition," *H.O. Publication* No. 225, Washington, D.C., **1944**, 48 maps.

vonder Haar, T. H., "Variations of the Earth's Radiation Budget," Ph. D. thesis, University of Wisconsin, Madison, **1969**, 118 pp.

Washington, Warren M., and Kasahara, Akira, "A January Simulation Experiment With the Two-Layer Version of the NCAR Global Circulation Model," *Monthly Weather Review*, Vol. 98, No. 8, Aug. **1970**, pp. 559–580.

White, Robert M., "The Counter-Gradient Flux of Sensible Heat in the Lower Stratosphere," *Tellus*, Vol. 6, No. 2, Stockholm, Sweden, May **1954**, pp. 177–179.

Yamamoto, G., "On a Radiation Chart," *Science Reports, Geophysics*, Ser. 5, Vol. 4, No. 1, Tohoku University, Sendai, Japan, June **1952**, pp. 9–23.

[Received July 21, 1970; revised November 24, 1970]